J Appl Physiol 133: 288–310, 2022.
First published June 23, 2022; doi:10.1152/japplphysiol.00089.2022

american physiological society | JOURNAL OF APPLIED PHYSIOLOGY

RESEARCH ARTICLE

A 3-D virtual human model for simulating heat and cold stress

Tushar Gulati,[1,2] Rajeev Hatwar,[1,2] Ginu Unnikrishnan,[1,2] Jose E. Rubio,[1,2] and Jaques Reifman[1]

[1]*Department of Defense Biotechnology High Performance Computing Software Applications Institute, Telemedicine and Advanced Technology Research Center, United States Army Medical Research and Development Command, Fort Detrick, Maryland and* [2]*The Henry M. Jackson Foundation for the Advancement of Military Medicine, Inc., Bethesda, Maryland*

Abstract

In this study, we extended our previously developed anatomically detailed three-dimensional (3-D) thermoregulatory virtual human model for predicting heat stress to allow for predictions of heat and cold stress in one unified model. Starting with the modified Pennes bioheat transfer equation to estimate the spatiotemporal temperature distribution within the body as the underlying modeling structure, we developed a new formulation to characterize the spatial variation of blood temperature between body elements and within the limbs. We also implemented the means to represent heat generated from shivering and skin blood flow that apply to air exposure and water immersion. Then, we performed simulations and validated the model predictions with experimental data from nine studies, representing a wide range of heat- and cold-stress conditions in air and water and physical activities. We observed excellent agreement between model predictions and measured data, with average root mean squared errors of 0.2°C for core temperature, 0.9°C for mean skin temperature, and 27 W for heat from shivering. We found that a spatially varying blood temperature profile within the limbs was crucial to accurately predict core body temperature changes during very cold exposures. Our 3-D thermoregulatory virtual human model consistently predicted the body's thermal state accurately for each of the simulated hot and cold environmental conditions and exertional heat stress. As such, it serves as a reliable tool to assess whole body, localized tissue, and, potentially, organ-specific injury risks, helping develop injury prevention and mitigation strategies in a systematic and expeditious manner.

NEW & NOTEWORTHY This work provides a new, unified modeling framework to accurately predict the human body's thermal response to both heat and cold stress caused by environmental conditions and exertional physical activity in one mathematical model. We show that this 3-D anatomically detailed model accurately predicts the spatiotemporal temperature distribution in the body under extreme conditions for exposures to air and water and could be used to help design medical interventions and countermeasures to prevent injuries.

cold injury; cold-water immersion; exertional heat stress; frostbite; hypothermia

INTRODUCTION

Heat- and cold-related injuries pose a significant threat to the health and safety of civilians (1, 2) and military personnel (3, 4). Heat illness, ranging from heat exhaustion to life-threatening heatstroke, results from a rise in the body's core temperature from prolonged exposures to hot and humid environments or from strenuous physical activity. In particular, severe heat illness hinders the body's thermoregulatory function, leading to multiple organ failure and eventual death (5). Likewise, cold injuries, such as hypothermia and frostbite, result from a decline in core and skin temperatures from extended exposure to cold air or water. Similar to heatstroke, hypothermia significantly impairs the body's thermoregulatory function, increasing the risk of cardiac arrhythmias and cardiac arrest (6), whereas frostbite causes freezing of the skin and the underlying tissues when the skin temperature falls below 0°C (7).

The progression from the initial thermal insult to a potential injury depends on the magnitude of the temperature of the core organs and tissues of the body and the peripheral skin (8, 9). Therefore, accurate characterization of the body's response to various thermal stressors can provide insights into the associated thermal-injury risks and the development of countermeasures for heat and cold stressors, enhancing clinical outcomes. However, because of ethical and safety concerns, we cannot conduct experiments on humans to characterize the body's response resulting from exposure to extreme heat or cold conditions, which might compromise the body's thermoregulatory system. One alternative is to use physics-based computational models that accurately mimic the body's thermoregulatory and physiological responses to predict the associated spatiotemporal temperature distribution under extreme conditions for which human experiments are not possible (10). In addition, by separately turning on/off different thermoregulatory mechanisms represented in such models, we

Correspondence: J. Reifman (jaques.reifman.civ@mail.mil).
Submitted 14 February 2022 / Revised 21 June 2022 / Accepted 21 June 2022

8750-7587/22 Published by the American Physiological Society.

could investigate the body's response to a compromised mechanism resulting from a severe thermal-stress exposure. Such a capability could provide the means to infer potential injury risks to susceptible organs and tissues from exposures to harsh environmental and operational conditions.

Over the years, several models of human thermoregulation have been proposed with varying levels of detail of the human anatomy and the body's thermoregulatory mechanisms [for review, see (11–13)]. By and large, the majority of the whole body thermoregulatory models approximate the body's anatomy by representing it as concentric cylinders or spheres. Although such approximations do not compromise the underlying physics, they lack the spatial resolution to predict the temperature response at the organ level and at the body's extremities. For example, although some cylinder-based models consider organ-level heat production [e.g., (14, 15)], they cannot capture the large temperature differences between the palm of the hand and those of the fingers in extreme-cold conditions (16), preventing their use in assessing frostbite and other nonfreezing cold injuries in vulnerable parts of the body. Recent advances in computational power have made it possible to develop three-dimensional (3-D) anatomically accurate models of the human body for simulating human thermoregulation (17–23). However, except for our recent efforts in which we considered both environmental conditions and exertional heat stress (20), and for the work of Zhang et al. (23), who reported an anatomically accurate finite-element model of the hand for extreme cold exposures, available models with realistic human anatomy have been limited to localized electromagnetic heating applications (18) or thermal-comfort research (21, 22). These works have not considered severe thermal-injury-risk scenarios, such as extreme cold stress in air or water and strenuous physical activity.

Currently available anatomically accurate models, including ours (20), lack the inherent capability to simulate extreme cold-stress conditions. This limitation arises from a simplification in the modeling formulation, which assumes a uniform blood temperature profile in the representation of internal convective heat transfer via the blood circulatory system. Although this assumption suffices for representing heat-stress scenarios, wherein the whole body heats up relatively uniformly (24), it may not be suitable for simulating severe cold-stress conditions. When exposed to cold, peripheral body elements lose heat faster than the core, owing to their large surface-to-volume ratio, resulting in a large temperature gradient between the body's periphery and internal organs (24). In addition, exposure to cold leads to a large temperature variation within the tissues of the extremities (25) and, because blood and the tissue are closely coupled, it leads to a spatially varying blood temperature profile throughout the body. Hence, to properly represent the body's response to cold stress, it is necessary to use a heat transfer formulation that accounts for such spatial variations in the blood temperature (14). Moreover, available whole body thermoregulatory models can simulate either cold-air exposure (11–13) or water immersion (26–28), but not both, under one unified modeling framework without introducing new model parameters or modifying existing ones, limiting their scope (15).

To address these limitations, we extended our recently developed 3-D thermoregulatory virtual human model to simulate exposure to both heat- and cold-stress conditions in air or water media within one modeling framework. The original model was developed to represent the thermal response of a 50th percentile US male exposed to environmental conditions and exertional heat stress, where validation results demonstrated its ability to accurately predict core and organ temperatures across a range of study conditions (20). In total, the model represents 25 metabolically active organs and tissues, as well as key thermoregulatory and heat-transfer mechanisms (Fig. 1*A*). Here, we developed a novel heat-transfer formulation capable of representing the spatial variation of blood temperature characteristic of cold stress, including partial capillary heat exchange, countercurrent heat exchange, and passing blood flow (PBF) heat exchange (see Fig. 1*A*, bullets in bold font, and Fig. 1*B*). We substituted our existing vasomotion formulation for regulating skin blood flow, which applies to air exposures only, with a formulation that is valid for both air and water exposures, and for each of these two media incorporated separate heat-generation mechanisms from shivering (i.e., a cold-stress response) as a heat source. In addition, to better represent external convective heat transfer in air and water, we updated our model with new correlations for estimating heat transfer coefficients during air exposure and included a coefficient for water immersion. Finally, we performed extensive model validation by comparing model predictions with measured experimental data for core body temperature, mean skin temperature, and heat due to shivering, encompassing cold-stress studies conducted in air (29–31) and water media (32–34). In addition, we revalidated our model predictions for heat-stress conditions (20, 35, 36), demonstrating the ability to have one unified thermoregulatory modeling framework that is applicable to a wide range of heat- and cold-stress scenarios.

MATERIALS AND METHODS

Experimental Studies

We calibrated and validated the extended 3-D virtual human model using rectal temperature, mean skin temperature, and shivering data collected from multiple cold-stress studies in air and water. In addition, we verified that the extended model replicated our previous predictions for heat-stress conditions (20), to ensure that the model applies to both heating and cooling scenarios. Table 1 summarizes the experimental studies used for model calibration (*study 1*) and model validation (*studies 2–10*). Briefly, these studies involved 70 unique male subjects exposed to 14 diverse conditions, ranging from extreme cold stress to strenuous physical activity in the heat and spanning diverse sets of ambient temperature (1°C–45°C), wind speed (0.1–2.5 m/s), relative humidity (30%–45%), clothing insulation (0.0–1.4 clo), and physical activity intensity [0.9–11.1 metabolic equivalent (MET)]. *Studies 1–7* consisted of cold-stress conditions, which

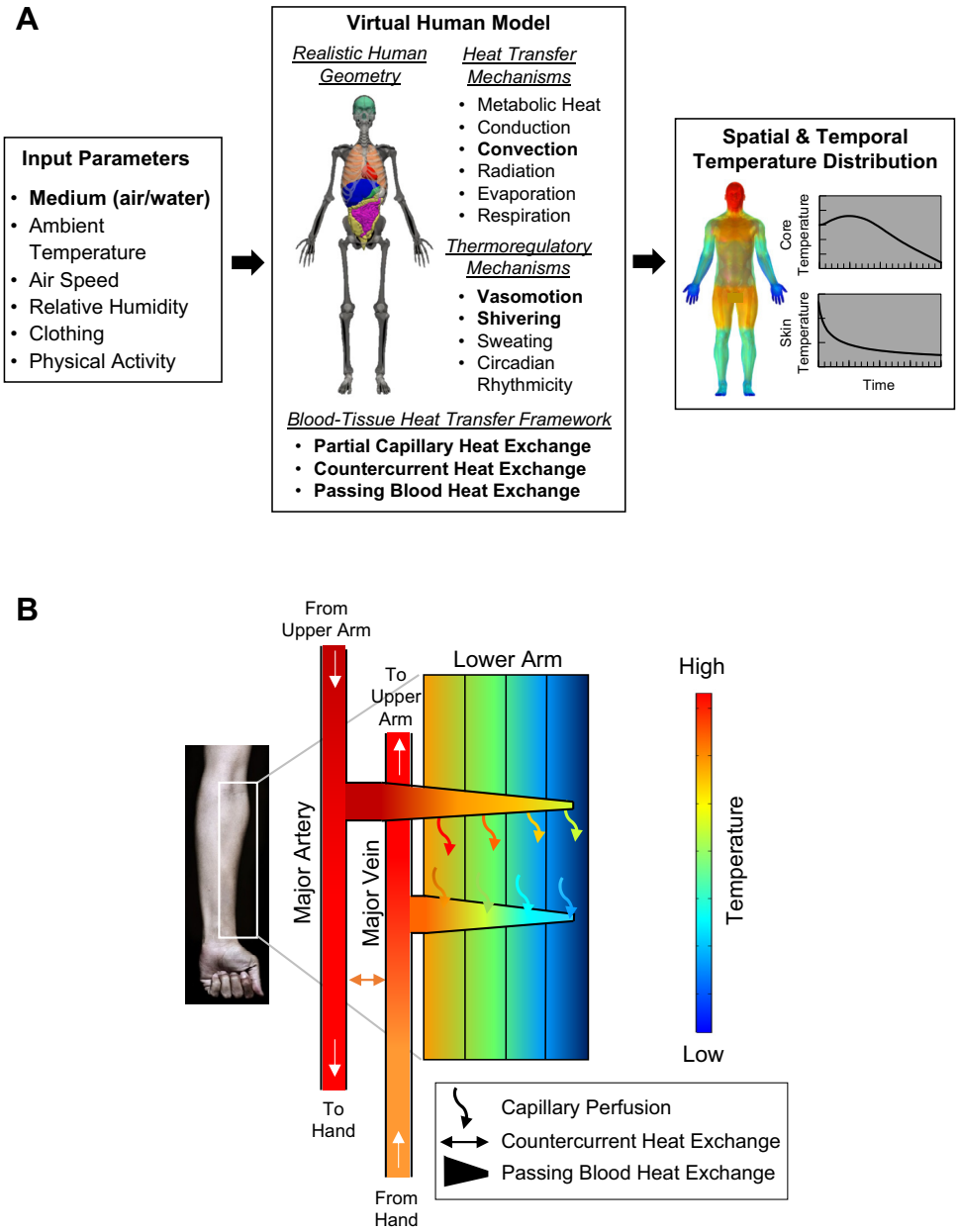

Figure 1. *A*: summary of new and existing thermal mechanisms represented in the extended three-dimensional thermoregulatory virtual human model. The extended model accounts for an anatomically accurate geometry; takes as inputs the surrounding medium (i.e., air or water), environmental conditions (i.e., atmospheric temperature, relative humidity, and wind speed), physical activity, and clothing; and predicts the spatiotemporal temperature distribution throughout the body, including 25 major organs and tissues. The model accounts for heat transfer within the body and between the body and the environment, including the major thermoregulatory mechanisms, circadian rhythmicity, and a novel blood-tissue heat transfer formulation. Bullets in bold font represent additional new physics incorporated into the extended model to enable for accurate simulations of cold-stress scenarios, beyond our previous implementation limited to heat-stress conditions (20). *B*: a schematic of the blood-tissue heat transfer formulation developed to estimate the blood temperature within the virtual human. The formulation includes *1*) blood perfusion at the level of the capillaries; *2*) countercurrent heat exchange between the major arterial and venous blood vessels; and *3*) passing blood flow heat exchange within a body extremity to account for the radially varying blood temperature profile.

included exposures to air (*studies 1–4*) (29–31) and immersion in water (*studies 5–7*) (32–34), whereas *studies 8–10* comprised environmental and exertional heat-stress challenges (20, 35, 36). We refer the reader to the original articles for additional information.

Computational Model

We previously developed and validated an anatomically accurate 3-D virtual human thermoregulatory model of a 50th percentile US male for heat stress (20). The model accounts for heat transfer within the body, heat exchange with the environment, and the primary physiological and thermoregulatory mechanisms regulating body temperature during heat stress. In the present study, we considerably extended the model by including additional physics related to the physiological and thermoregulatory mechanisms of cold stress (Fig. 1*A*, bullets in bold font). In particular, we extended the modified Pennes bioheat transfer equation (PBHE) by including *1*) partial heat exchange at the capillary level; *2*) countercurrent heat exchange between arterial and venous temperature within the body; and *3*) convective heat exchange between the PBF and the tissue, preceding capillary perfusion. In addition, as part of the thermoregulatory mechanisms, we included heat generated due to shivering for exposures to cold air and water and replaced our previous skin blood flow formulation, which was only valid for air exposure, with an approach that applies to both air and water.

Energy balance.

To obtain the spatiotemporal temperature distribution within the body, we extended the modified PBHE (24, 38) and solved the energy balance for the time-dependent temperature T, as follows:

$$\underbrace{\rho c_p \frac{\partial T}{\partial t}}_{\text{Heat storage}} = \underbrace{\nabla \cdot k \nabla T}_{\text{Heat conduction}} + \underbrace{\beta \rho_b c_{p,b} \dot{\omega}_b (T_a - T)}_{\text{Capillary perfusion}} + \underbrace{\chi \rho_b c_{p,b} (\dot{p}bf)(T_a + T_v - 2T)}_{\text{Passing blood flow heat exchange}} + \underbrace{\dot{Q}_{met}}_{\text{Metabolic heat}} + \underbrace{\dot{Q}_{Act}}_{\text{Activity heat}} + \underbrace{\dot{Q}_{Sh}}_{\text{Shivering heat}} \quad (1)$$

We obtained the density ρ, specific heat capacity c_p, thermal conductivity k, blood perfusion rate $\dot{\omega}_b$, and $\dot{Q}_{met}$ for the different organs and tissues from the literature (see Table A1 in the APPENDIX) (39–42). We used a value of 0.7 for the coefficient β, which accounts for the partial heat exchange between the perfusing arterial blood and the tissues at the extremities, i.e., the arms, hands, legs, and feet (43). In addition, using the data from Bittel et al. (29), we estimated the PBF heat exchange efficiency χ as 0.9 via a model-calibration exercise.

Blood-tissue heat transfer.

Heat exchange via the circulating blood is the primary mode of heat transfer within the body. The blood and tissues are intricately connected by the vascular system, which transcends multiple length scales. During cold exposure, there is a considerable temperature difference between the various body elements and within the body extremities. Therefore, the assumption of a uniform blood temperature in the entire body, particularly during cold stress, is an oversimplification that leads to an incorrect prediction of the body's thermal state. To overcome this limitation, we developed a blood-tissue heat transfer formulation to account for the spatial blood temperature variation within the body and implemented it in the virtual human model (Fig. 1*B*). This formulation provided a more realistic description of the blood temperature in the virtual human and replaced our previous formulation that assumed a uniform blood temperature throughout the body (20).

First, to account for the spatial variation of blood temperature between body elements, we explicitly included the blood flow paths from the heart to the extremities and back and invoked the countercurrent heat-exchange mechanism to obtain different arterial and venous blood temperatures in the 12 body elements in Table 2 (14, 45). Second, to characterize the radial spatial variation in blood temperature within the extremities (38), we included the convective heat exchange from the PBF above the capillary level.

Countercurrent heat exchange. To compute the arterial blood temperature $T_{a,i}$ and the venous blood temperature $T_{v,i}$ in each of the ith elements of the body, i = 1, 2, ... 12, we represented the major arteries and veins of each element as two distinct reservoirs, applied a countercurrent heat exchange between them, and solved the energy balance for $T_{a,i}$ and $T_{v,i}$, as follows:

$$\underbrace{M_{a,i} \frac{dT_{a,i}}{dt}}_{\text{Rate of energy accumulation}} = \underbrace{\dot{m}_{a,in,i} c_{p,b} T_{a,in,i} - \dot{m}_{a,out,i} c_{p,b} T_{a,out,i}}_{\text{Net rate of energy transfer by the incoming and outgoing blood}} + \underbrace{h_{ccx,i}(T_{v,in,i} - T_{a,in,i})}_{\text{Countercurrent heat exchange}} - \underbrace{\left(\int \rho_b c_{p,b} \dot{\omega}_{b,i} dV_i \right) T_{a,i}}_{\text{Capillary perfusion heat exchange}} \quad (2)$$

$$M_{v,i} \frac{dT_{v,i}}{dt} = \dot{m}_{v,in,i} c_{p,b} T_{v,in,i} - \dot{m}_{v,out,i} c_{p,b} T_{v,out,i} + h_{ccx,i}(T_{a,in,i} - T_{v,in,i}) + \left(\int \rho_b c_{p,b} \dot{\omega}_{b,i} dV_i \right) \left(\beta T_{a,i} + (1 - \beta) \overline{T}_i \right) \quad (3)$$

To satisfy the mass flow rate and temperature continuity at the junction between two successive body elements, the solutions to *Eqs. 2* and *3* required additional auxiliary equations, which are summarized in the APPENDIX (*Eqs. A1–A8*). Table 2 lists the parameter values for the 12 body elements associated with *Eqs. 2* and *3*.

This formulation results in a uniform blood temperature distribution within each body element. However, for the

Table 1. *Experimental studies used for calibrating and validating the three-dimensional virtual human thermoregulatory model*

Study	Condition	No. of Subjects	Ambient Temperature, °C	Duration, min	Air Speed, m/s	Humidity		Clothing			Activity Type	Activity Intensity, MET	Source
						Relative, %	Absolute, kPa	Type	Local Intrinsic Insulation, clo[c]	Whole Body Insulation, clo[c]			
							Cold Stress						
							Air exposures						
1[a]	Extreme cold	17	1	120	0.8	40	0.3	Trunks	0.6	0.05	Reclining	0.9	(29)
2[b]	Very cold	17	5, 10	120	0.8	40	0.3, 0.5	Trunks	0.6	0.05	Reclining	0.9	(29)
3	Moderate cold	9	12, 17	60	0.1	45	0.6, 0.9	Trunks	0.6	0.05	Sitting	1.0	(30)
4	Moderate, mild cold	8	15, 20	120	0.4	40	0.7, 0.9	Shorts	0.6	0.05	Reclining	0.9	(31)
							Water immersion						
5	Very cold-very hot	5	10–40	60–30				Wet Trunks	0.0	0.0	Sitting	1.0	(33)
6	Very cold, temperate	8	15, 25	135				Wet Trunks	0.0	0.0	Sitting	1.0	(34)
7	Mild cold	8	20	120				Wet Trunks	0.0	0.0	Sitting	1.0	(32)
							Heat Stress						
8	Neutral-very hot	5	29–45–29–45	30–30–30–30	0.1	40	1.6, 3.8	Shorts	0.6	0.05	Sitting	1.0	(36)
9	Exertional heat	3	30	210	0.1	30	1.3	Shorts	0.6	0.05	Ergometer cycling	3.0–8.0	(35)
10	Exertional heat	7	36	420	2.5	30	1.8	T-shirt/shorts/ socks/ shoes	0.4/0.6/1.3/1.4	0.29	Treadmill running	4.2–11.1	(20)

[a]*Study 1* used for model calibration. [b]*Studies 2–10* used for model validation. [c]Obtained from Ref. 37. MET, metabolic equivalent.

limbs, such as the arms and legs, which show a significant temperature variation between their core and peripheral regions during cooling (25), it is unlikely that such a uniform representation would be accurate. Therefore, for the limbs, we varied the blood temperature radially within these body elements by invoking the PBF heat-exchange mechanism (38).

Passing blood flow heat exchange. Figure 1*B* illustrates the passing blood convective heat exchange in the limbs using the lower arm as an example. According to this formulation, the blood in the artery flows radially toward the skin through the various muscle compartments of the limb and exchanges heat with the tissue (shown by the trapezoid) before perfusing at the capillary level (shown by the curved arrows). As a result, there is a progressive drop in the arterial temperature within the limb from the innermost (hot) to the outermost (cold) muscle compartment, and the extent of this drop is determined by the PBF heat exchange efficiency χ in *Eq. 1*. Similarly, the venous blood temperature progressively increases as it flows from the outer to the inner tissue layers.

For these calculations, we divided the muscle tissue in each limb into four compartments. *Equations 4–9* describe the arterial and venous blood temperatures in the jth muscle compartment, with j = 1 (innermost), …, 4 (outermost), of the ith limb element, while accounting for the PBF heat exchange:

$$T_{a,in,i,j} = T_{a,out,i,j-1} \tag{4}$$

$$T_{a,i,j} = T_{a,in,i,j} \tag{5}$$

$$T_{a,out,i,j} = \chi \overline{T}_{i,j} + (1-\chi) T_{a,i,j} \tag{6}$$

$$T_{v,in,i,j} = T_{v,out,i,j+1} \tag{7}$$

$$T_{v,i,j} = \frac{\dot{\omega}_{b,i,j}[\beta \overline{T}_{i,j} + (1-\beta) T_{a,i,j}] + \dot{pbf}_{i,j} T_{v,in,i,j}}{\dot{\omega}_{b,i,j} + \dot{pbf}_{i,j}} \tag{8}$$

$$T_{v,out,i,j} = \chi \overline{T}_{i,j} + (1-\chi) T_{v,i,j} \tag{9}$$

where $\dot{pbf}_{i,j}$ represents the amount of the PBF through a compartment, which is obtained as:

$$\dot{pbf}_{i,j} = \sum_{j+1}^{N} \dot{\omega}_{b,i,j} \tag{10}$$

For the innermost layer, the arterial blood entered the compartment at $T_{a,i}$, computed using *Eq. 2*, and the venous blood drained into the major (central) vein at $T_{v,out,i,1}$, which we implemented by replacing the expression $\left(\beta T_{a,i} + (1-\beta)\overline{T}_i\right)$ in *Eq. 3* with $T_{v,out,i,1}$ in *Eq. 9*.

Skin blood flow.

We implemented a phenomenological formulation for regulating skin blood flow (SBF) and accounted for vasoconstriction and vasodilation during exposures to air and water. Previously (20), we used Fiala's SBF model (46, 47), i.e., an empirical formulation limited to air exposures only, where he obtained the various coefficients by fitting model-predicted core and skin temperatures with experimental data based on the geometry of an "average" human. Although our virtual human model accurately predicted heat-stress responses

Table 2. *Parameters used in the blood-tissue heat transfer formulation*

Body Element [i]	Countercurrent Heat Exchange Coefficient [$h_{ccx,i}$] W·K^{-1}	Passing Blood Efficiency [χ]	Partial Blood Perfusion Coefficient [β]	Arterial Blood Thermal Mass [$M_{a,i}$], J·K^{-1} [a]	Venous Blood Thermal Mass [$M_{v,i}$], J·K^{-1} [a]
Head	0.0	0.0	1.0	446.0	1,365.7
Face	0.0	0.0	1.0	243.2	744.3
Neck	0.0	0.0	1.0	121.6	372.0
Thorax	0.0	0.0	1.0	2,267.0	6,942.0
Abdomen	0.0	0.0	1.0	567.0	1,736.0
Upper leg	1.6	0.9	0.7	93.0	285.0
Lower leg	5.9	0.9	0.7	37.0	113.0
Feet	1.5	0.0	0.7	19.0	57.0
Shoulder	0.0	0.0	0.0	19.9	60.4
Upper arm	1.2	0.9	0.7	30.1	91.5
Lower arm	3.0	0.9	0.7	37.0	99.0
Hand	0.6	0.0	0.7	21.0	66.0

[a]Obtained from Ref. 44.

using Fiala's SBF model, we obtained unsatisfactory predictions when simulating cold-stress conditions. Instead of going through a time-intensive, laborious fitting exercise to obtain new coefficients for this formulation for both heat- and cold-stress conditions, we instead used the SBF model proposed by Wissler (15, 48, 49). Wissler's SBF model is based on experimentally observed changes in SBF encompassing a large number of studies, uses coefficients that are not confined to a particular geometry, and has been successfully used for predicting the body's thermal response during exposures to both air and water (15, 50). We summarized Wissler's model in the APPENDIX (*Eqs. A9–A15*) and provide SBF and convective heat transfer coefficient parameters in Table 3. We refer the reader to the original articles for a detailed derivation of the SBF model.

Shivering.

We used two separate formulations, one for air and another for water, to represent shivering as a source of heat in the model.

Air exposure. We modified the equation for predicting heat due to shivering for air exposure $\dot{S}h_{air}$ reported by Timbal et al. (31) so as to capture this phenomenon during extreme cold-air exposures reliably. Following their work, we included *1*) the initial rapid rise in shivering for the first ~30 min of cold exposure based on the rate of change of the mean skin temperature ($dT_{sk,m}/dt$) and *2*) the gradual increase in shivering thereafter based on the drop in the mean skin temperature from the thermoneutral condition $\Delta T_{sk,m}$. For $t \leq 30$ min, we found that their relationship was adequate for accurately predicting the initial rapid rise in shivering. However, for $t > 30$ min, we updated the $\dot{S}h_{air}$ versus $\Delta T_{sk,m}$ correlation provided by Timbal et al. (31) to include additional experimental datasets (29, 54–56), which covered extreme cold-stress conditions (see Fig. A1 in the APPENDIX). Using the updated correlation, we obtained the following relationship to estimate the total heat from shivering during cold-air exposure:

$$\dot{S}h_{air} = \underbrace{7.6 - 109.8\frac{dT_{sk,m}}{dt} - 1.9\Delta T_{sk,m}}_{\text{Initial rise in shivering}} + \underbrace{0.36\ \Delta T_{sk,m}{}^{2} + 10.27\ \Delta T_{sk,m} - 25.08}_{\text{Gradual increase in shivering}} \quad (11)$$

Water immersion. We represented the heat from shivering during water immersion $\dot{S}h_{water}$ as a function of the core body temperature T_c and the mean skin temperature $T_{sk,m}$. Accordingly, this formulation accounts for the heat generated during the immersion phase (15, 57) as well as postimmersion, including rewarming (33):

Table 3. *Skin parameters for blood flow and convective heat transfer*

Body Element [i]	Skin Thickness, mm[a]	Skin Perfusion, s^{-1} [b]	Natural Convection Coefficient [N_i][c]	Forced Convection Coefficient [C_i][d]	Forced Convection Exponent [e_i][d]
Head	2.1	5.7E-3	1.96	6.1	0.50
Face	2.1	5.7E-3	1.96	6.1	0.50
Neck	2.1	5.7E-3	1.96	6.1	0.50
Thorax	2.8	1.4E-4	1.64	9.1	0.59
Abdomen	2.6	5.6E-4	1.86	8.2	0.65
Upper leg	2.5	7.5E-4	2.24	8.9	0.56
Lower leg	2.5	2.9E-4	2.24	13.4	0.56
Feet	3.4	7.0E-4	2.24	13.4	0.56
Shoulder	2.8	3.8E-4	1.58	11.6	0.66
Upper arm	2.6	4.1E-4	1.58	11.9	0.63
Lower arm	2.6	3.4E-4	2.02	11.9	0.63
Hand	2.8	1.4E-4	2.02	11.9	0.63

[a]Obtained from Ref. 51. [b]Obtained from Ref. 44. [c]Obtained from Ref. 52. [d]Obtained from Ref. 53.

$$\dot{Sh}_{water} = \begin{cases} \dfrac{\left[-155(37 - T_c) - (1.6(28 - T_{sk,m}) - 47)(30 - T_{sk,m})\right]}{\sqrt{BF}} A_{sk}, & \dfrac{dT_{sk,m}}{dt} < 0 \\ 2.4(T_{sk,m} - 42.2)(T_c - 41.4) - 82.5, & \dfrac{dT_{sk,m}}{dt} \geq 0 \end{cases} \quad (12)$$

We distributed the heat from shivering obtained using *Eq. 11* or *Eq. 12* to the muscle tissues of the torso and the upper limbs, as follows: 49% thorax, 26% legs, 22% abdomen, and 3% arms (58, 59).

Boundary conditions.

We included convection, radiation, evaporation, and respiration to describe the heat exchange of the virtual human with the environment. In addition, we included the effects of clothing on the convective and evaporative modes of heat transfer (see the APPENDIX for a brief description of the *Clothing Model*). We refer the reader to our previous work for details on the implementation of the various boundary conditions (20). Here, we only describe the changes we made to our original formulation. For estimating the heat transfer coefficient h_c during air exposure, we used the correlations proposed by de Dear et al. (53) and Wissler (52), as follows:

$$h_c = \begin{cases} N_i(T_{sk,i} - T_{air})^{0.25}, & v_{air} < 0.2 \text{ m/s} \\ C_i(v_{air})^{e_i}, & 0.2 \text{ m/s} \leq v_{air} \leq 5.0 \text{ m/s} \end{cases} \quad (13)$$

as we found them to result in better predictions of $T_{sk,m}$ at high wind-speed conditions, over our previous formulation. Table 3 summarizes the coefficient values (N_i, C_i, and e_i) for the various body elements to obtain h_c during air exposures. For water immersion, we used an average h_c value of 210 $W \cdot m^{-2} \cdot K^{-1}$ (28).

Model setup and initialization.

To obtain the spatiotemporal temperature distribution in the virtual human, we used the commercially available finite-element software package COMSOL Multiphysics (COMSOL, Burlington, MA). Our previous work (20) details geometry creation, mesh generation, and mesh and time-step convergence studies.

To determine the initial temperature distribution throughout the body, we initialized the model at a thermoneutral condition [i.e., 28°C ambient air, 0.1 m/s wind speed, 40% relative humidity, and the subject wearing shorts (0.6 clo) and reclining (0.8 MET)]. When simulating the thermoneutral condition, we switched on vasodilation and vasoconstriction to regulate the dry heat loss from the body via SBF changes and turned off the evaporation and sweating responses (60). In addition, we adjusted the countercurrent heat exchange coefficients from Fiala and colleagues (40, 47) and Ferreira and Yanagihara (61) to obtain an initial core body (rectal) temperature $T_{c,0}$ of 37°C and a mean skin temperature $T_{sk,m0}$ of 34°C, which we used as baseline values for subsequent calculations.

RESULTS

Calibration of the PBF Heat Exchange Efficiency and Initial Validation

Calibration of the PBF efficiency χ.

We estimated the value of the parameter χ in *Eqs. 1, 6*, and *9* to represent the efficiency of the PBF heat exchange during cold stress through a model-calibration procedure. To this end, we used experimental data from an extreme cold-stress study conducted at a 1°C air exposure (*study 1*, Table 1) (29). Figure 2 shows the experimental data (solid circles) along with the predicted changes in core body temperature ΔT_c (Fig. 2*A*), mean skin temperature $T_{sk,m}$ (Fig. 2*B*), and heat generated from shivering $\dot{Sh}_{air}$ (Fig. 2*C*) for χ ranging from 0.3 to 0.9. We found that the predictions of ΔT_c were very sensitive to the choice of χ and improved with larger values of χ. In contrast, $T_{sk,m}$ and $\dot{Sh}_{air}$ were unaffected by the choice of χ. In addition, to assess the benefit of the PBF heat-exchange mechanism in the model predictions, we computed ΔT_c while considering only the countercurrent heat mechanism without the PBF mechanism (Fig. 2*A*, black dashed line). Without the PBF, we observed a considerable under prediction of ΔT_c (−1.7°C at the end of the 120-min exposure), highlighting the importance of including this mechanism in a whole body model to accurately predict changes in core temperature resulting from cold stress. Based on this analysis, we set χ = 0.9 for subsequent calculations, including model validations based on *studies 2–10* in Table 1.

Initial validation of $T_{sk,m}$ and $\dot{Sh}_{air}$.

Because the thermoregulatory responses $T_{sk,m}$ and $\dot{Sh}_{air}$ were not sensitive to χ, we used the comparisons between their predictions with the measured data in Fig. 2, *B* and *C* as an initial validation of the model for an extreme cold-stress scenario. The model correctly predicted the temporal variation of $T_{sk,m}$ and $\dot{Sh}_{air}$ over the entire 120-min exposure, with root mean squared errors (RMSEs) of 1.2°C and 28 W, respectively. Using a 3.4-GHz 4-core Intel i7 Workstation with 64 GB RAM, we completed a 120-min simulation in 48 h of central processing unit time.

Estimated Blood Temperatures in the Extremities

We computed the arterial and venous blood temperatures to illustrate their spatial variation with and without the PBF mechanism. Figure 3 shows the simulated blood temperature profiles at the start (t = 0 min, thermoneutral condition) and at the end (t = 120 min) of the extreme cold-stress experiment in *study 1* (Table 1), using χ = 0.9. As expected, at both time points, the predicted arterial blood

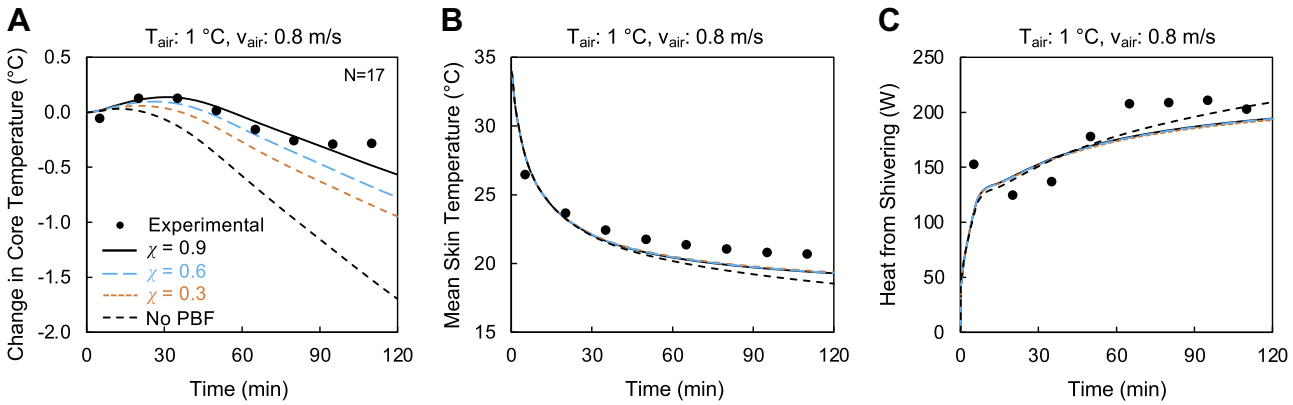

Figure 2. Model calibration to estimate the value of the passing blood flow (PBF) efficiency χ, using data from the extreme cold-stress condition in *study 1* (1°C ambient temperature T_{air} and 0.8 m/s wind speed v_{air}, Table 1). Shown are the average values of the experimental data along with the model-predicted changes in core body temperature (*A*), mean skin temperature (*B*), and heat generated from shivering (*C*), as a function of different values of χ (0.3, 0.6, and 0.9), as well as predictions without the PBF mechanism. Experimental measurement uncertainty was not available for *study 1*. *N*, number of subjects.

temperatures (Fig. 3, *A* and *B*) and venous blood temperatures (Fig. 3, *C* and *D*) progressively decreased from the body's core regions to the extremities. In addition, with the PBF mechanism for the limbs, we observed a progressive decline in blood temperature from the center to the outer layers of the limbs (Fig. 3, *A–D*, *right*). The most striking effect of the PBF mechanism was the elevated venous blood temperature returning from the limbs to the core (Fig. 3*D*, *right*), which helped prevent the rapid drop in the predicted ΔT_c response, as compared with the model without it (Fig. 3*D*, *left*, and Fig. 2*A*). This result reinforced the importance of incorporating the PBF mechanism, in addition to countercurrent heat exchange, to adequately estimate changes in core temperature resulting from exposure to cold-stress conditions.

Model Validation

We validated the extended virtual human model by comparing model-predicted ΔT_c, $T_{sk,m}$, and $\dot{S}h$ with experimental data collected during cold-air exposure and cold-water

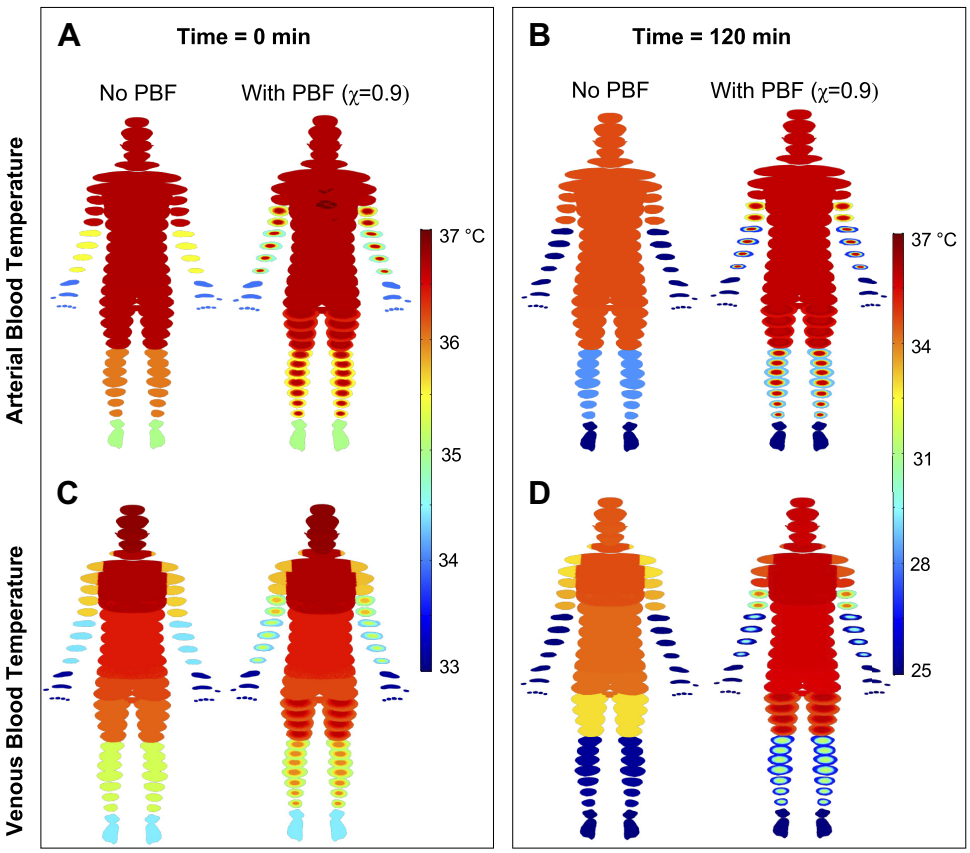

Figure 3. Simulated spatial variation of blood temperature within the three-dimensional virtual human model for the extreme cold-stress condition in *study 1* (ambient temperature of 1°C and wind speed of 0.8 m/s) at the beginning (t = 0 min, *A* and *C*) and at the end (t = 120 min, *B* and *D*) of the simulation. (Note that we used different color scales to illustrate the temperature distribution at the two time points.) Each of the four panels illustrates the blood temperature variation with and without the passing blood flow (PBF) mechanism for the arterial vessels (*A* and *B*) and venous vessels (*C* and *D*). Note the spatial variation of blood temperatures within the arms and legs and a higher venous blood return temperature from the limbs to the core for the model that considers the PBF mechanism.

immersion. In addition, we revalidated our model predictions for environmental and exertional heat-stress challenges to ensure that the extended model applied to both heating and cooling scenarios.

Cold-air exposures.

We compared our model-predicted responses with measured data obtained during cold-air exposures to mild, moderate, and extreme cold environments, with ambient air temperatures ranging from 5°C to 20°C, wind speeds from 0.1 to 0.8 m/s, and subjects wearing minimal clothing (*studies 2–4*, Table 1). We observed a very good agreement between model-predicted responses and experimental measurements for each of the six different cold-stress conditions in the three studies, with RMSEs ranging between 0.0°C and 0.2°C for core temperature change ΔT_c (Fig. 4), 0.3°C and 1.2°C for mean skin temperature $T_{sk,m}$ (Fig. 5), and 6 and 29 W for heat generated from shivering $\dot{S}h_{air}$ (Fig. 6). Importantly, our model accurately predicted both the trend and magnitude of these variables, illustrating its ability to capture various thermoregulatory responses for a range of cold-air exposures.

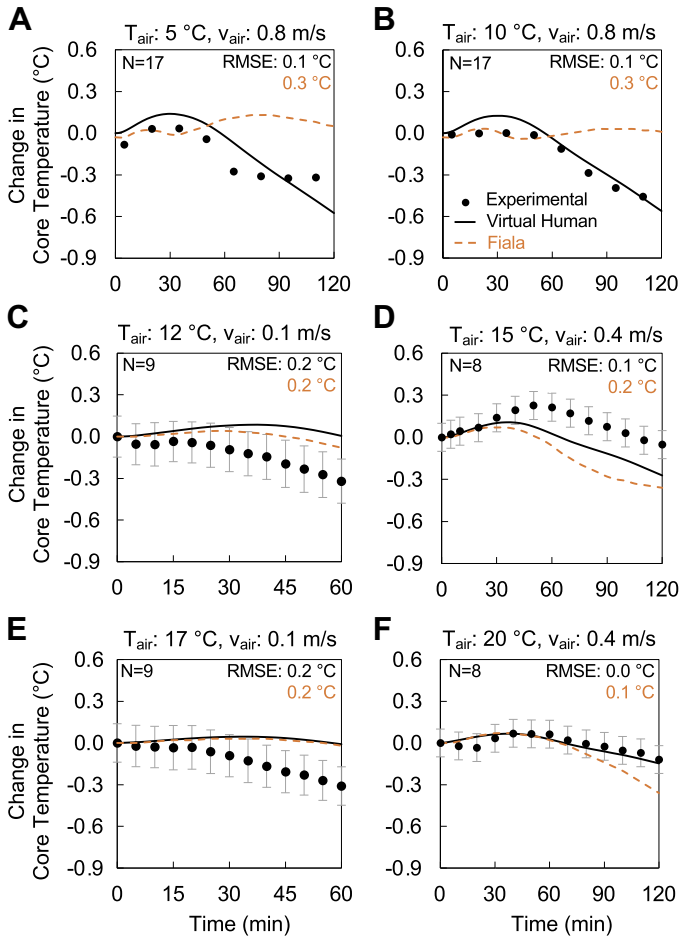

Figure 4. Model validation of the core body temperature for mild, moderate, and very cold environmental conditions in *study 2* (*A* and *B*), *study 3* (*C* and *E*), and *study 4* (*D* and *F*), while subjects sat quietly for 60 or 120 min wearing minimal clothing (Table 1). The filled circles represent the average of the measured changes in core body temperature values, the vertical gray bars indicate two standard errors of the mean (not available for *study 2*), and the solid black lines denote the changes predicted by the virtual human model. The orange dashed lines represent the predictions based on the Fiala model (40, 46). RMSE, root mean squared error; T_{air}, ambient temperature; v_{air}, wind speed. *N*, number of subjects.

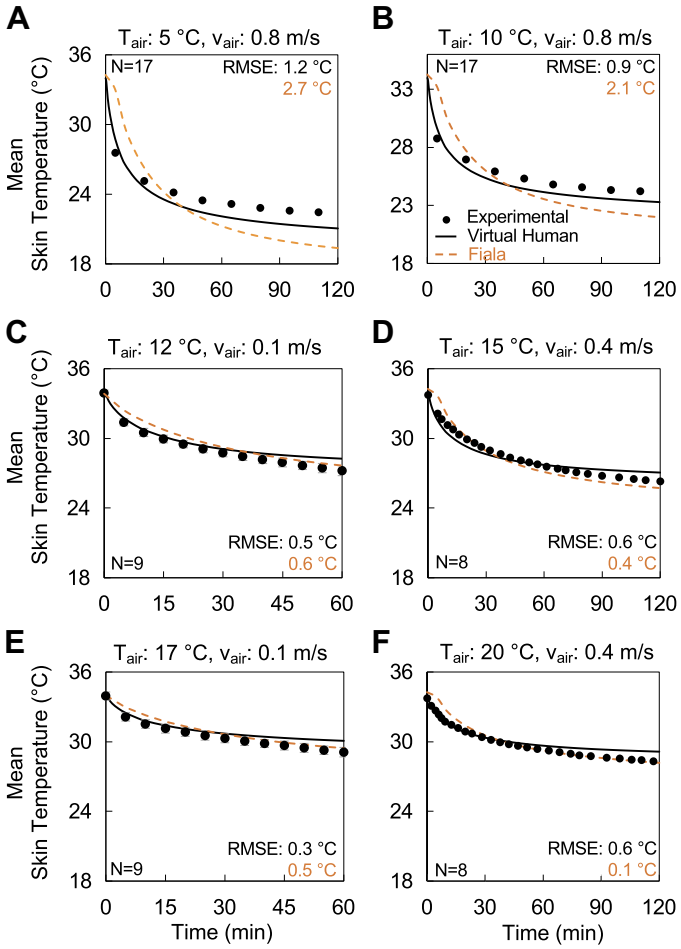

Figure 5. Model validation of the mean skin temperature for mild, moderate, and very cold environmental conditions in *study 2* (*A* and *B*), *study 3* (*C* and *E*), and *study 4* (*D* and *F*), while subjects sat quietly for 60 or 120 min wearing minimal clothing (Table 1). The filled circles represent the average of the measured mean skin temperature values, and the solid black lines denote the changes predicted by the virtual human model. Experimental measurement uncertainty was not available for *studies 2* and *4* and is not visible for *study 3*. The orange dashed lines represent the predictions based on the Fiala model (40, 46). RMSE, root mean squared error; T_{air}, ambient temperature; v_{air}, wind speed. *N*, number of subjects.

In general, the predicted ΔT_c exhibited an initial rise followed by a gradual decline (Fig. 4). The initial rise resulted from the combination of three factors: *1*) a rapid reduction in SBF due to vasoconstriction, which prevented warm blood from reaching the skin and losing heat to the environment; *2*) heat recovery by the returning venous blood via a partial heat exchange with the tissue at the capillary level, PBF heat exchange above the capillary level, and countercurrent heat exchange with the major arteries; and *3*) an initial increase in shivering $\dot{S}h_{air}$ (Fig. 6). Thereafter, the heat loss by conduction from the extremities to the environment resulted in a drop in the venous blood temperature returning to the core and a decline in ΔT_c. In terms of $T_{sk,m}$, it dropped rapidly as soon as the body was exposed to the cold environment,

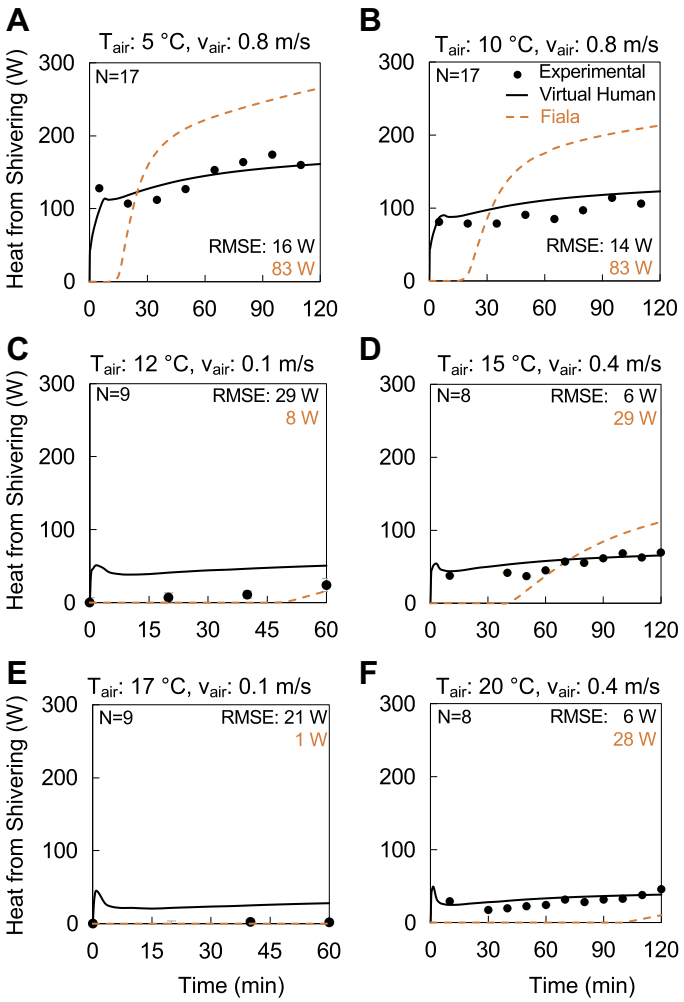

Figure 6. Model validation of the heat generated from shivering for mild, moderate, and very cold environmental conditions in *study 2* (*A* and *B*), *study 3* (*C* and *E*), and *study 4* (*D* and *F*), while subjects sat quietly for 60 or 120 min wearing minimal clothing (Table 1). The filled circles represent the average of the measured heat generated from shivering, and the solid black lines denote the changes predicted by the virtual human model. Experimental measurement uncertainty was not available for *studies 2* and *4* and is not visible for *study 3*. The orange dashed lines represent the predictions based on the Fiala model (40, 46). RMSE, root mean squared error; T_{air}, ambient temperature; v_{air}, wind speed. *N*, number of subjects.

due to a strong convective and radiative heat loss to the ambient air, followed by a more gradual drop (Fig. 5). The predicted $\dot{S}h_{air}$ showed a sharp initial peak associated with the large rate of decrease in $T_{sk,m}$, followed by a sustained increase until the end of the cold-stress period (Fig. 6). Notably, our model correctly captured the changes in skin temperature for a wide range of cold-air exposures, during which the body is more susceptible to frostbite injuries in the peripheral body regions.

Cold-water immersion.

We compared the model-predicted ΔT_c, $T_{sk,m}$, and $\dot{S}h_{water}$ with experimental data from three separate water-immersion studies (*studies 5–7*, Table 1). We observed very good agreement between model predictions and experimental measurements for each of the three studies, with RMSEs ranging between 0.1°C and 0.5°C for ΔT_c (Fig. 7), 1.0°C and 2.6°C for $T_{sk,m}$ (Fig. 8), and 29 and 74 W for $\dot{S}h_{water}$ (Fig. 9). Most notably, for *study 5*, which involved rewarming the subjects after immersion in very cold water, the model predictions of ΔT_c followed the experimental data closely for the entire duration of the experiment (Fig. 7*A*). In addition, our model successfully captured the timing and amplitude of the "after-drop" phenomenon during rewarming (times between 60 and 90 min in Fig. 7*A*), wherein the core body temperature continued to drop for ~15 min into the rewarming phase. In agreement with the experiments, the predicted $T_{sk,m}$ dropped rapidly during cooling and rose almost immediately during rewarming due to the high heat exchange with the surrounding water (Fig. 8*A*). Although our model predictions of $\dot{S}h_{water}$ for *study 5* closely matched the measured data during the cold-water immersion phase, we observed some discrepancies during the rewarming phase (Fig. 9*A*). In the experiment, shivering continued to occur for a certain duration after rewarming began, however, our simulations did not adequately capture this response. This discrepancy resulted from a limitation of the shivering model, as noted by the original model developers (15, 33, 57).

Unlike cold-air exposures, the decline in ΔT_c during cold-water immersion was more substantial (up to −2.6°C vs. −0.5°C for cold-air exposures), increasing with a decrease in water temperature. For *studies 6* and *7*, which involved prolonged water immersions (≥120 min), ΔT_c showed an S-curve behavior (Fig. 7, *B–D*), dropping gradually due to a continual loss of body heat to the surrounding water and then stabilizing thereafter due to an increase in shivering activity. As in *study 5*, the $T_{sk,m}$ dropped rapidly during the first few minutes of the immersion, and then plateaued just above the water temperature (Fig. 8, *B–D*). The shivering response showed an initial rapid rise concomitant with the rapid drop in $T_{sk,m}$. Thereafter, shivering steadily increased due to a drop in core body temperature (Fig. 9, *B–D*).

Heat-stress studies.

To confirm the ability of the extended model to predict a human response for heat-stress conditions, we simulated one environmental (*study 8*) and two exertional heat-stress scenarios (*studies 9 and 10*), with subjects exposed to very hot environments, wearing different clothing ensembles, and performing activities of varying levels. Similar to our original work, the model successfully captured the temporal dynamics and magnitude of ΔT_c and $T_{sk,m}$ over the entire duration of each of the three experiments, with RMSEs ranging between 0.1°C and 0.3°C (see Figs. A2 and A3 in the APPENDIX).

Skin Temperature Variation in the Hand during Cold-Air Exposure

We estimated the skin temperature distribution of the hand to illustrate the model's ability to predict spatio-temporal variations of the palm, dorsum hand, and fingertips for the extreme cold-stress condition in *study 1*. Figure 10*A* shows a very good agreement between the virtual human's dorsum hand temperature predictions

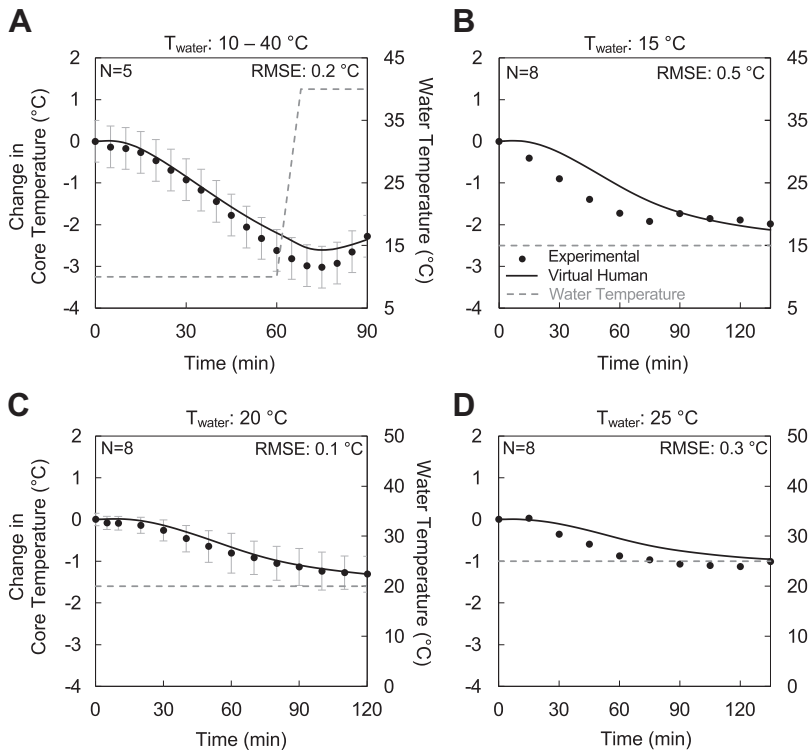

Figure 7. Model validation of the changes in core body temperature collected during water-immersion experiments in *study 5* (*A*, very cold to very hot), *study 6* (*B* and *D*, very cold and temperate, respectively), and *study 7* (*C*, mild), with subjects immersed up to the neck level and sitting quietly for 90 to 135 min while wearing minimal clothing (Table 1). The filled circles represent the average of the measured changes in core body temperature values, the vertical gray bars indicate two standard errors of the mean (not available for *study 6*), the dashed gray lines indicate the water temperature, and the solid black lines denote the core temperature changes predicted by our virtual human model. RMSE, root mean squared error; T_{water}, water temperature. *N*, number of subjects.

(solid black line) and the experimental measurements (RMSE of 1.3°C). In addition, Fig. 10*A* shows the computed temperature temporal variation of the index fingertip (dashed black line), which was markedly lower than that of the dorsum hand by as much as ~8.0°C, reaching the threshold for nonfreezing cold injury to set in (~5.0°C). Figure 10*B* shows the spatial temperature distribution of the hand at the end of the 120-min exposure period, indicating a ~5°C difference between the palm of the hand and the fingertips.

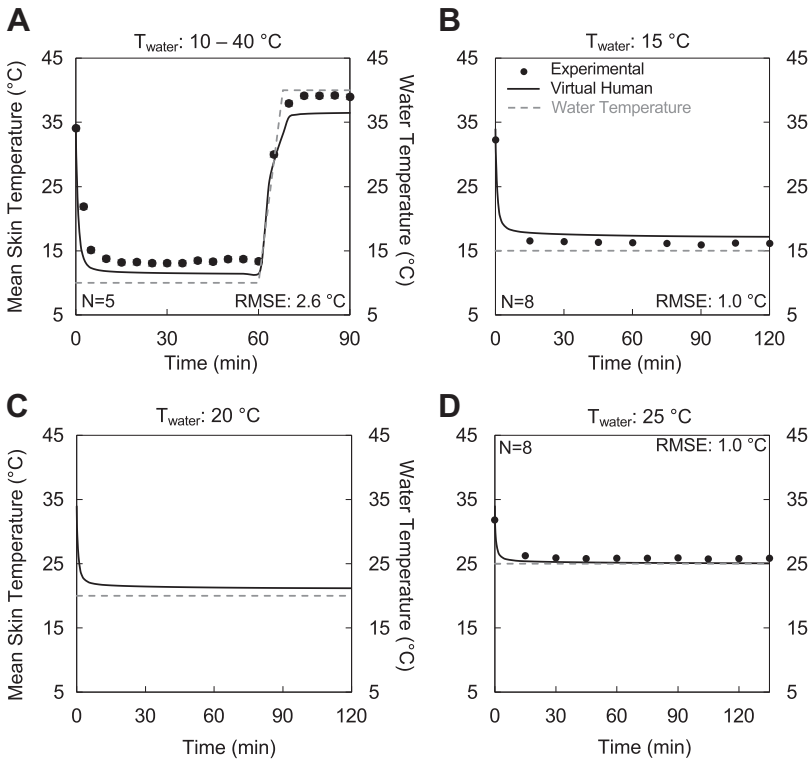

Figure 8. Model validation of the mean skin temperature collected during water-immersion experiments in *study 5* (*A*, very cold to very hot), *study 6* (*B* and *D*, very cold and temperate, respectively), and *study 7* (*C*, mild), with subjects immersed up to the neck level and sitting quietly for 90 to 135 min while wearing minimal clothing (Table 1). The filled circles represent the average of the measured mean skin temperature values, the dashed gray lines indicate the water temperature, and the solid black lines denote the mean skin temperatures predicted by our virtual human model. Experimental data were not available for *study 7*, and measurement uncertainty was not available for *study 6* and is not visible for *study 5*. RMSE, root mean squared error; T_{water}, water temperature. *N*, number of subjects.

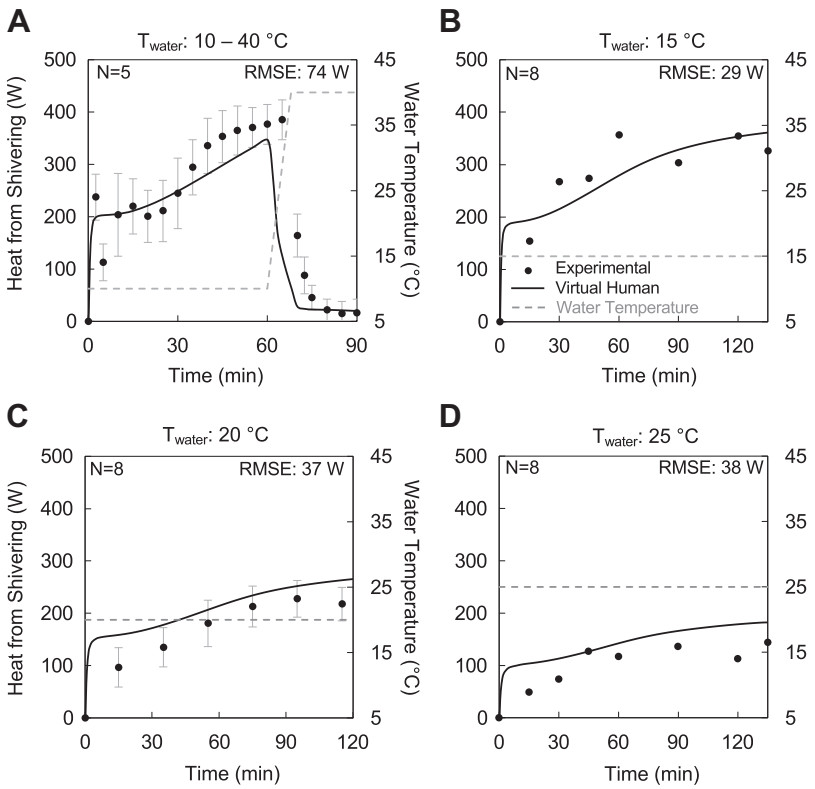

Figure 9. Model validation of the heat generated from shivering collected during water-immersion experiments in *study 5* (*A*, very cold to very hot), *study 6* (*B* and *D*, very cold and temperate, respectively), and *study 7* (*C*, mild), with subjects immersed up to the neck level and sitting quietly for 90 to 135 min while wearing minimal clothing (Table 1). The filled circles represent the average of the measured heat generated from shivering, the vertical gray bars indicate two standard errors of the mean (not available for *study 6*), the dashed gray lines indicate the water temperature, and the solid black lines denote the heat generated from shivering as predicted by our virtual human model. RMSE, root mean squared error; T_{water}, water temperature. *N*, number of subjects.

Predicted Spatial Temperature Distribution in the Body during Cold-Water Immersion

Figure 11 shows the model-predicted spatial temperature distributions of the skeletal system and the internal organs before (Fig. 11*A*) and after (Fig. 11*B*) immersion in 10°C water for the conditions in *study 5*. Before immersion, the temperature of all internal organs was ~37°C (Fig. 11*A*, *right*). In the skeletal system, the bones of the hands and feet were at a lower temperature (~33.5°C) than those of the arms and legs (~35.7°C; Fig. 11*A*, *left*). After 60 min of cold-water immersion, the temperature of different organs reached distinct lower values (Fig. 11*B*, *right*). The extent of such temperature decrease depended on the organ's *1*) heat-transfer properties, such as density, blood perfusion rates, and basal metabolic heat; *2*) proximity to the skin, which favored heat loss via conduction to the cold water; and *3*) proximity to muscle groups, which generated shivering-induced heating. We predicted the lowest

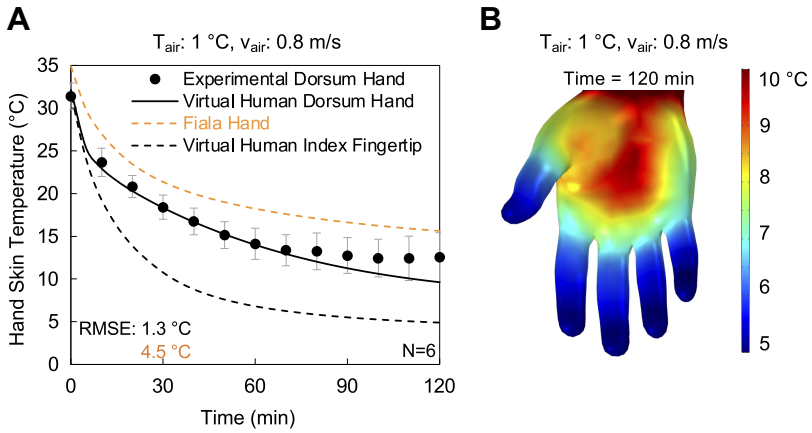

Figure 10. *A*: model validation of the dorsum hand temperature and fingertip temperature for the extreme cold-stress condition in *study 1*, in which subjects sat bare-handed at 1°C air temperature (T_{air}) and 0.8 m/s wind speed (v_{air}) for a period of 120 min while wearing trunks (Table 1). The filled circles represent the average of the measured dorsum hand temperature, the vertical gray bars indicate two standard errors of the mean, the solid and dashed black lines denote the dorsum hand and fingertip temperature predictions from the virtual human model, respectively, and the orange dashed line represents the hand skin temperature predicted by the Fiala model (40, 46). The latter model provides one lumped-parameter value for the entire hand, as it does not have the spatial resolution to distinguish different parts of the hand. *B*: model-predicted spatial temperature distribution of the hand at the end of the exposure for the conditions described in *A*. Note the large differences in temperature between the palm of the hand and the fingertips. RMSE, root mean squared error. *N*, number of subjects.

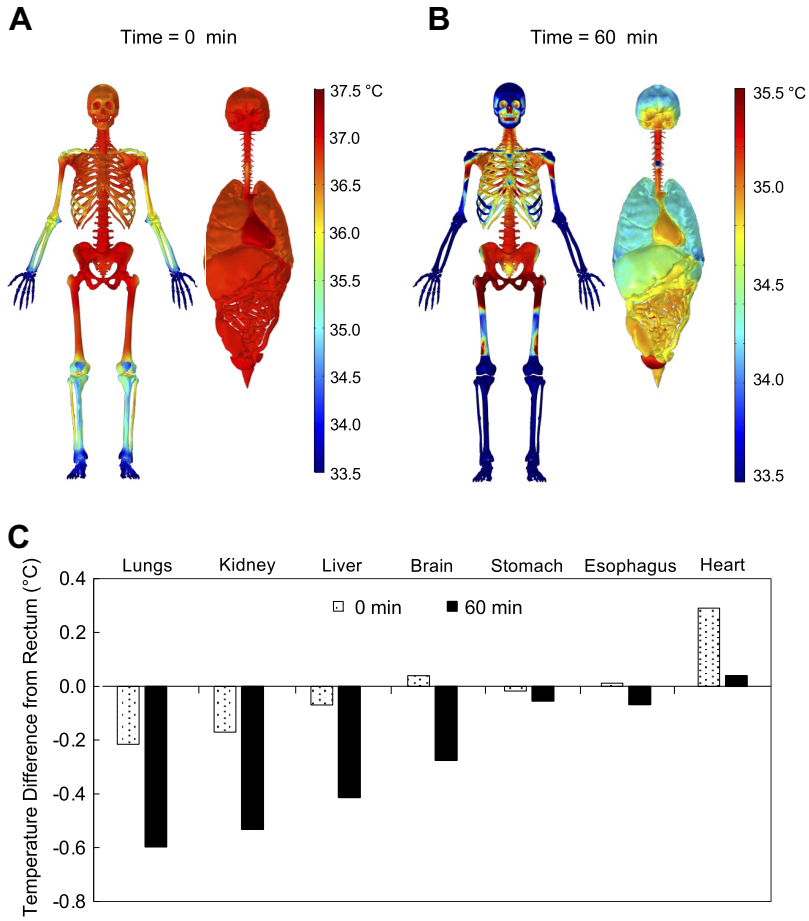

Figure 11. Simulated spatial temperature distribution of the skeletal system and the internal body organs before (t = 0 min, *A*) and after (t = 60 min, *B*) the whole body immersion in 10°C water in *study 5* (Table 1). Because of the different temperature ranges at the two time points, to highlight the temperature changes, we used different color scales for panels *A* and *B*. In each of the two panels, we represented the skeletal system on the left and the body organs on the right. *C*: simulated temperature differences of various organs with respect to the rectum pre- (t = 0 min) and postimmersion (t = 60 min) in 10°C water. A negative value indicates that the organ temperature was lower than that of the core.

average temperatures in the lungs (~34.3°C) and observed slightly higher values for the other internal core organs, such as the stomach, intestines, and the heart (~35.0°C). Although we simulated water immersion up to the neck level (i.e., head-out immersion), we observed that the temperature in the brain still decreased due to internal convection via the circulating cold blood from the core. In the skeletal system, the bones of the thorax, abdomen, and upper legs maintained higher temperatures than those of the bones in the peripheral regions of the body primarily because of their proximity to shivering-generating muscle groups. In addition, peripheral bones experienced a more significant external convective heat loss to the cold water (Fig. 11*B*, *left*).

Figure 11*C* shows the temperature difference between various internal organs and the core (as predicted in the rectum) before and after the cold-water immersion. At preimmersion (i.e., at t = 0 min), all organs except for the heart were either at approximately the same or at a slightly lower temperature than the core. At postimmersion (i.e., at t = 60 min), the lungs, kidney, liver, and brain temperatures dropped at an average of ~0.5°C below the rectal temperature. Surprisingly, we did not observe a larger variation in temperature among the internal organs.

DISCUSSION

In this study, we extended our previously developed anatomically detailed 3-D thermoregulatory virtual human model validated for heat stress by adding new physics to simulate cold stress (Fig. 1*A*). The extended model replaces our previous uniform blood-temperature formulation with a new methodology that accounts for the spatially varying blood temperature profiles in arteries and veins between 12 major body elements and within the limbs, with the skin in contact with either air or water (Fig. 1*B*, Tables 2 and 3). In addition, the extended model incorporates new formulations for representing shivering, vasoconstriction, vasodilation, and external convective heat transfer coefficients to reliably capture the body's thermoregulatory responses during cold stress. In contrast, previously developed whole body models represent the human body as stacks of concentric cylinders, where lumped-parameter blood temperatures only vary between cylindrical elements, where the cylinder representing the skin is surrounded by either air (11) or water (26–28), except for Wissler's model (15). More recent thermoregulatory models, with a realistic anatomical representation of the human body similar to ours, use the simplified uniform blood-temperature formulation, which limits the use of the model to environmental heat-stress and mild cold-air exposures (21, 22). In addition, unlike the 3-D virtual human model, these models have not been applied to simulate exertional heat stress, which is the major driver for increases in body temperature during exposure to hot and humid environments (~95%) (20, 35).

Blood temperature is the primary factor that controls heat transfer within the body, driving internal convection and

redistribution of heat from the core to the periphery. During exertional heat stress, the warm blood convects the exertional heat from the working muscles to the skin, wherein the heat dissipates to the surrounding environment. Likewise, during cold stress, a large temperature difference exists between the body core and skin, and the blood temperature plays a pivotal role in regulating the core body temperature. In particular, although the skin temperature approaches its cool surroundings, the core temperature attempts to maintain normothermia around 37°C, leading to large spatial temperature variations between and within the various parts of the body. To account for this phenomenon and adequately estimate the thermal response to cold-stress conditions, we developed a new mathematical formulation of the circulatory system. Our blood temperature-estimation formulation describes the flow of energy of the circulating blood from the major arteries and veins to the various body elements and includes: *1*) countercurrent heat exchange between the major artery-vein pairs; *2*) radial PBF heat exchange in the limbs above the capillary perfusion level; and *3*) partial heat exchange in capillary perfusion. Figure 2*A* illustrates the improved accuracy achieved by including these three spatial blood-temperature variation mechanisms for the extreme cold-stress condition in *study 1* (Table 1). By including the PBF mechanism, the model-predicted core body temperature ΔT_c (solid black line) closely followed the experimental data, in stark contrast to a simulation that accounted for the countercurrent heat exchange but excluded the PBF heat exchange (dashed black line). None of the whole body models in the literature accounts for such a radial blood temperature distribution within the body.

We estimated χ in *Eqs. 1, 6*, and *9* using the extreme cold condition in *study 1* and calibrating for the corresponding core body (rectal) temperature data ΔT_c (Fig. 2*A*). The use of rectal temperature as a valid index of core body temperature is a subject of debate for certain conditions, such as cold-water immersion (62, 63). However, most experimental studies report rectal temperature data. Therefore, we used this index to calibrate χ and validate our model predictions, while recognizing that our estimated χ could vary depending on the core temperature index used for calibration. In our virtual human model, we set χ to 0.9, meaning that the arterial and venous blood temperatures approach 90% of the local tissue temperature as they flow through the limbs. In this process, as the major artery branches out before reaching the capillary bed, the arterial blood temperature progressively decreases by depositing heat into colder tissues (Fig. 3*B*, *right*). Conversely, the venous blood flows from the outermost tissue layers after capillary perfusion and progressively increases in temperature by recovering the heat deposited in the tissue by the arterial blood. As a consequence, the venous blood reaches the major vein at a higher temperature, preventing rapid cooling of the body core (Fig. 3*D*, *right*). In contrast, when we assume a uniform blood temperature across the entire limb and do not allow for heat exchange between the blood and tissue above the capillary perfusion level, the heat deposition mechanism by the arterial blood and the subsequent recovery by the venous blood are absent (Fig. 3, *A–D, left*). Accordingly, the venous blood reaches the central vein at a relatively lower temperature, causing excess core cooling and a more significant drop in the model-predicted core body temperature than observed in the experiments or predicted by the PBF mechanism (Figs. 2*A* and 3*D*, *left*).

As noted by Tikuisis and Ducharme (38), a few localized tissue models describe a continual decrease in the arterial blood temperature as it flows out from the main supply and vice versa for the venous return (64, 65). However, these efforts did not investigate the impact of a spatially varying blood temperature in the limbs on the prediction of core body temperature. Our assessment highlights the need to account for such a variation in a whole body thermoregulatory model to correctly describe the thermal response within the body and obtain accurate predictions of core body temperature changes when simulating cold-stress conditions.

We validated the extended virtual human model for multiple cold-stress exposures in air and water by comparing experimental measurements and model predictions of ΔT_c, $T_{sk,m}$, and $\dot{S}h$. For cold-air exposures (*studies 2–4*), our model tracked the measured values well for each of the three thermoregulatory responses, including: *1*) the initial rise in T_c observed in most experimental studies (Fig. 4); *2*) the entire temporal profile of $T_{sk,m}$ (Fig. 5); and *3*) the sharp initial rise in $\dot{S}h_{air}$ observed during some cold-stress studies (Fig. 6). We did observe some discrepancies between our predicted $\dot{S}h_{air}$ response and the observed trend in *study 3* (Fig. 6*C*), in which the subjects did not exhibit a shivering response when exposed to 12°C cold air. However, a similar experimental study also conducted at 12°C air (66) reported shivering values of ~30 ± 25 W (means ± 2SE) at 60 min into the study, which compares favorably well with our model-predicted response (~50 W) at that time point. The large between-subject variability in anthropometric measurements, skin surface area, body-fat percentages, and acclimation status could help explain some of the observed discrepancies between experimental studies, as well as the disagreement between our predictions of shivering and the experimental values. Nonetheless, overall, we observed a very good agreement between model predictions and experimental measurements, indicating that our model can adequately predict the thermal response of the body resulting from cold-air exposures.

To demonstrate the benefit of the extended 3-D virtual human model, we repeated the simulations for cold-air exposures (*studies 2–4*) using the cylinder-based Fiala model (13, 20) and contrasted its predictions with both the measured data and our 3-D model predictions. To this end, we used JBODY [Energy Simulation Solutions Ltd., Loughborough, UK; (67)], a publicly available online implementation of the Fiala model (40, 46), after ensuring that this implementation reproduced the published results for various heat and cold exposures simulated by Fiala et al. (46). For the very cold condition in *study 2* (Fig. 4, *A* and *B*), the virtual human model yielded a RMSE of 0.1°C, whereas Fiala's model yielded threefold larger errors (0.3°C). More importantly, our model-predicted trend of ΔT_c closely tracked the experimental data, whereas Fiala's did not vary for the entire duration of the experiment. For the moderate-to-mild cold-stress conditions in *studies 3* and *4*, respectively, the two models yielded comparable predictions (Fig. 4, *C–F*).

For $T_{sk,m}$, when compared with Fiala's results, we again observed lower errors in our model predictions for *study 2* conducted at low T_{air} and high v_{air} (RMSEs of 0.9°C–1.2°C vs. 2.1°C–2.7°C; Fig. 5, *A* and *B*), with the model predictions satisfying the acceptable error criterion of <1.6°C for estimating $T_{sk,m}$ (10). For the relatively higher values of T_{air} and lower values of v_{air} in *studies 3* and *4*, the prediction errors of both models were small and acceptable (<1°C; Fig. 5, *C–F*). Finally, when comparing the predicted $\dot{S}h_{air}$ response, we observed a sizeable difference between Fiala's model predictions and the experimental measurements (Fig. 6, *A*, *B*, and *D*). The model-predicted $\dot{S}h_{air}$ showed significant variability, from predicting no shivering (although subjects shivered in the experiments) to estimating more vigorous shivering than the experimental observations. Most notably, for *study 2*, Fiala's model predicted a twofold increase in $\dot{S}h_{air}$ from the observed response (Fig. 6, *A* and *B*), which could explain, in part, its elevated ΔT_c response (Fig. 4, *A* and *B*). In contrast, the 3-D model predicted $\dot{S}h_{air}$ with good accuracy. The better predictions of the 3-D model for low T_{air} and high v_{air} values are due to *1*) an improved blood-temperature estimation formulation, which more accurately predicts the body's core temperature; *2*) the new correlations for obtaining the external convective heat transfer coefficient at high wind speeds; and *3*) the updated shivering model for extreme cold-stress conditions. Overall, these comparisons highlight the importance of the proposed modeling formulation in the simulation of cold and very cold environmental conditions.

For cold-water immersion in *studies 5–7*, our model-predicted thermoregulatory responses closely matched the trends and values observed in the experiments (Figs. 7, 8, and 9). Importantly, we obtained these results while using the same model used for simulating cold-air exposures, except for the replacement of the convective heat transfer coefficient h_c and the shivering formulation from air in *Eq. 11* to water in *Eq. 12*. In contrast, with the exception of Wissler (15), existing thermoregulatory models are either applicable to cold-air exposures (11) or cold-water immersion (27, 28), but not both. It is not clear whether, and to what extent, these models can be used across different surrounding media without modifying model parameters and model formulation. When Wissler simulated exposures to both air and water, he reported making ad hoc changes to the model when switching between the two media (15). Specifically, he initiated vasoconstriction in the inactive (nonshivering) muscle groups during air exposure to reduce the flow of warm blood to these muscles and reduce heat loss to the environment, which prevented a rapid drop in the model-predicted ΔT_c response. Then, he reversed this mechanism when simulating water immersion to facilitate a large drop in ΔT_c, as observed in experiments. However, as stated by Wissler (15), there is no experimental evidence to support these ad hoc changes to the model. In contrast, our changes in h_c and $\dot{S}h$ are systematic and guided by physical principles. These results demonstrate that the proposed modeling formulation is equally applicable to cold-air exposure and cold-water immersion and capable of providing insights into the physiology and pathophysiology of a wide range of cold-stress conditions.

To ensure that the new modeling formulation did not affect the ability to simulate exertional and environmental heat-stress conditions, we revalidated the extended model using *studies 8–10* (Table 1). Indeed, the model predictions for ΔT_c and $T_{sk,m}$ responses showed an excellent agreement with the measurements of each of the three studies, both in magnitude (RMSEs of 0.1°C–0.3°C) and temporal dynamics, despite the significant variations in ambient temperature and physical activity intensity in the studies (see Figs. A2 and A3). During heat stress, the spatial temperature distribution within the body is relatively uniform, resulting in similar arterial and venous blood temperatures. Consequently, the effects of countercurrent and the PBF heat exchange, which are key heat-recovery mechanisms by the venous blood during cold stress, are automatically diminished for heat stress (24, 25). Importantly, when simulating these heat-stress cases, we did not turn off any mechanism in our new formulation. Rather, we simply changed the input conditions to mimic the experimental studies. These results demonstrate that the extended model is general, being equally applicable to predict the body's thermal response to both heating and cooling, while using one unified modeling formulation.

Our anatomically accurate model can spatially characterize the temperatures of the peripheral body regions that are most prone to frostbite during cold-air exposures and predict the onset times for frostbite and other nonfreezing injuries, including the loss of hand dexterity. Cylinder-based models cannot provide such details, because they lack geometric resolution and can only predict one lumped skin temperature value representative of the entire hand or foot. For example, our model accurately predicted the skin temperature in the body's extremities, such as the dorsum hand in *study 1* (RMSE of 1.3°C, Fig. 10*A*), and accounted for the considerable spatial temperature variations between the dorsum, palm, and fingertips, where the latter approached very low temperatures during extreme cold-stress conditions (Fig. 10*B*). In contrast, Fiala's cylinder-based model is only able to predict an average skin temperature on the hand, which showed significant deviations from the measured dorsum temperature (RMSE of 4.5°C, Fig. 10*A*). This result highlights the importance of using a realistic anatomical representation of the human body to facilitate the development of countermeasures to reduce the risk of cold injuries in civilians and military personnel, including, but not limited to, the design of novel hand- and feet-warming devices (68), evaluation of clothing insulation requirements for various cold-exposure conditions (69), development of real-time decision aids that predict the onset of frostbite and nonfreezing cold injuries as well as the loss of hand dexterity during cold-weather operations (70), and assessment of the ability of external heat-warming devices to prevent trauma-induced hypothermia (71).

Our extended model can also characterize thermal responses at the organ level. Although core body temperature is routinely measured and taken as an indicator of hypothermia, our model is capable of predicting the temperature distribution in the major organs. For example, during the cold-water immersion (i.e., head-out immersion) in *study 5* (Table 1), the model predicted that the brain cooled as much as other internal organs due to the cold blood flow from the core. It predicted an average drop in brain temperature of ~2.9°C at the core temperature nadir (Fig. 7*A*), which

represents an additional ~0.3°C drop compared with the rectum (Fig. 11*B*). Under hypothermic conditions, a lower brain temperature, due to a decrease in the metabolic demand of the brain tissues, is beneficial to preserve organ integrity (72, 73). This hypothermia-induced cerebral protection has been successfully used to perform brain and heart surgeries and prevent hypoxic brain damage (74). Because in vivo measurements of brain temperature are challenging, our model provides the capability to estimate brain temperature for various therapeutic hypothermic applications and could be used to help design medical interventions (75) and surgical procedures (76, 77). Although it would have been desirable to validate the predicted organ temperatures against experimental data, unfortunately, the lack of organ-specific temperature measurements under extreme scenarios precluded such validation. In our previous study (20), we successfully validated the model predictions for various organs under thermoneutral conditions, demonstrating its ability to accurately capture organ-specific thermal responses under those conditions. These results suggest that the model could be used to predict more extreme conditions, as long as the corresponding thermoregulatory mechanisms are represented in the modeling framework. For example, during cold-induced hyperventilation, the body's response to protect the brain tissues from damage is to sharply reduce cerebral perfusion (78), a mechanism not represented in the current model. In such a case, because our model is physics-based, we could readily incorporate such localized thermoregulatory mechanism to account for organ-specific thermal responses, provided that we have sound and extensive experimental data on the underlying mechanism. Nonetheless, in its current state, we recommend caution when using our model-predicted organ temperatures for making certain clinical decisions.

Our model has limitations. First, it uses the geometry of a 50th percentile US male with the palm of the hands open and the fingers extended, as illustrated in Figs. 1*A* and 10*B*. Therefore, it cannot explicitly account for variations in anthropometric measurements, body surface area, body fat percentages among individuals, or unique hand configurations, like a fist. To account for such variability and configurations in a future extension of the model, we would need to acquire medical images and reconstruct the 3-D geometry for specific population groups and cases. Moreover, we do not know the extent to which our model is applicable to female subjects. In the near future, we intend to develop a thermoregulatory model for a 50th percentile US female, using a similar approach as for the virtual human male model. Second, our model does not consider acclimatization or the acclimation effects of the human body to heat or cold stress, and the associated changes in vasomotion as well as shivering and sweating responses. In principle, we could account for heat and cold adaptation by modifying the model, for example, by simply updating the model equations and associated parameters representing the various thermoregulatory responses. However, the limitation arises from the lack of mathematical model formulations that accurately represent such habituation effects. In addition, we did not incorporate centrally and locally mediated redistribution of blood perfusion between deep and superficial veins in response to changes in core body and skin temperatures. However, the exclusion of this mechanism did not seem to have affected our predictions of the body's thermal response under different heat- (or cold-) stress scenarios. Third, although the model adequately predicted the hand skin temperature for an extreme cold-stress study, we need to perform additional assessments of the model predictions for localized skin temperatures, including the face, fingers, and toes, as well as exposures to subzero temperatures and exercise conditions in the cold, as a follow-up validation effort. Such validation shall further demonstrate the feasibility of using the virtual human model to predict cold-injury risks. Finally, our model does not account for variations in blood flow to the visceral organs during thermal stress. During extreme cold stress or while performing strenuous physical activity in the heat, blood is redirected to the participating muscle groups to meet the metabolic demands of the muscle tissues. Consequently, blood flow, and hence convective heat transport, to the core organs is reduced, likely affecting their temperatures. However, in our model, we do not account for the redistribution of blood volume, which may explain, in part, the similarity in our model-computed organ temperatures. Despite such limitations, we observed a good agreement between model predictions and experimental measurements from multiple studies conducted in air and water, and in the heat and cold, justifying our assumptions in the development of the 3-D thermoregulatory virtual human model.

Conclusion

In this study, we advanced our previously developed 3-D virtual human model for heat stress (20) to enable simulations of cold-stress scenarios, with the skin in contact with air or water. Specifically, we extended the uniform blood-tissue heat transfer formulation, which included only capillary perfusion, to incorporate the additional mechanisms of countercurrent and PBF heat exchange and allow for the representation of a spatially varying blood temperature profile characteristic of cold stress. We found that these mechanisms strongly affect the core temperature predictions during cold-stress simulations. We improved upon our previous formulations for regulating SBF, heat generated from shivering, and external convective heat transfer coefficients, which enabled us to obtain accurate predictions of mean skin temperature and heat generated from shivering when simulating cold-air exposures. To generalize our model, we implemented the means to simulate human exposure to cold-water immersion, which only requires changes in the external heat transfer coefficient and the use of the shivering model for water, and confirmed our model's ability to accurately predict heat-stress conditions. We validated the model against experimental data from multiple studies, highlighting the ability to represent a broad range of thermal-stress scenarios under one unified modeling framework. In summary, our results demonstrate that the 3-D thermoregulatory virtual human model can serve as a powerful tool to identify whole body, localized-tissue, and, potentially, organ-specific injury risks, helping the development of new and improved thermal-injury prevention and mitigation strategies.

GLOSSARY

A_{sk}	Skin surface area (m^2)
AVD	Active vasodilation (dimensionless)
BF	Body fat (%)
c_p	Specific heat capacity ($J \cdot kg^{-1} \cdot K^{-1}$)
$c_{p,b}$	Specific heat capacity of blood ($J \cdot kg^{-1} \cdot K^{-1}$)
C	Forced convection coefficient (dimensionless)
C_{sbf}	Circadian function for skin blood flow (dimensionless)
CVCM	Centrally mediated vasoconstriction (dimensionless)
CVCL	Locally mediated vasoconstriction (dimensionless)
e	Forced convection exponent (dimensionless)
f^*_{cl}	Local clothing area factor (dimensionless)
h_c	Convective heat transfer coefficient ($W \cdot m^{-2} \cdot K^{-1}$)
h_{ccx}	Countercurrent heat exchange coefficient ($W \cdot K^{-1}$)
h_r	Radiative heat transfer coefficient ($W \cdot m^{-2} \cdot K^{-1}$)
i	Index for body element (dimensionless)
i^*_{cl}	Local moisture permeability index of clothing layer (dimensionless)
I^*_{cl}	Local thermal resistance of clothing layer ($W^{-1} \cdot m^2 \cdot K$)
j	Index for muscle compartment in a limb (dimensionless)
k	Thermal conductivity ($W \cdot m^{-1} \cdot K^{-1}$)
$\dot{m}_{a,in}$	Incoming arterial blood mass flow rate ($kg \cdot s^{-1}$)
$\dot{m}_{a,out}$	Outgoing arterial blood mass flow rate ($kg \cdot s^{-1}$)
$\dot{m}_{v,in}$	Incoming venous blood mass flow rate ($kg \cdot s^{-1}$)
$\dot{m}_{v,out}$	Outgoing venous blood mass flow rate ($kg \cdot s^{-1}$)
m_{sw}	Sweat mass (kg)
M_a	Thermal mass of arterial blood ($J \cdot K^{-1}$)
M_v	Thermal mass of venous blood ($J \cdot K^{-1}$)
n	Number of body elements along a blood flow path (dimensionless)
N	Natural convection coefficient (dimensionless)
pbf	Passing blood perfusion rate ($m^3 \cdot s^{-1} \cdot m^{-3}$)
p_{air}	Partial water vapor pressure of surrounding air (Pa)
$p_{osk,sat}$	Saturated partial water vapor pressure within the outer skin layer (Pa)
p_{sk}	Partial water vapor pressure at skin surface (Pa)
$\dot{Q}_{Act}$	Activity heat generation per unit volume of tissue ($W \cdot m^{-3}$)
$\dot{Q}_{Met}$	Metabolic heat generation per unit volume of tissue ($W \cdot m^{-3}$)
$\dot{Q}_{Sh}$	Shivering heat generation per unit volume of tissue ($W \cdot m^{-3}$)
$R_{E,sk}$	Skin moisture resistance ($W^{-1} \cdot m^2 \cdot Pa$)
$SBF_{i,0}$	Basal skin blood perfusion rate ($m^3 \cdot s^{-1} \cdot m^{-3}$)
SBF_i	Skin blood perfusion rate dependent on time ($m^3 \cdot s^{-1} \cdot m^{-3}$)
$\dot{Sh}_{air}$	Total heat from shivering during air exposure (W)
$\dot{Sh}_{water}$	Total heat from shivering during water immersion (W)
T	Body temperature dependent on spatial location and time (°C)
$\bar{T}$	Volume-averaged tissue temperature (°C)
T_a	Arterial blood temperature (°C)
$T_{a,in}$	Incoming arterial blood temperature (°C)
$T_{a,out}$	Outgoing arterial blood temperature (°C)
T_{air}	Ambient air temperature (°C)
T_{amb}	Ambient operative temperature (°C)
$T_{c,0}$	Baseline core body temperature (°C)
T_c	Core body temperature (°C)
$T_{c,th,0}$	Baseline threshold core body temperature for active vasodilation (°C)
$T_{c,th}$	Threshold core body temperature for active vasodilation (°C)
T_v	Venous blood temperature (°C)
$T_{v,in}$	Incoming venous blood temperature (°C)
$T_{v,out}$	Outgoing venous blood temperature (°C)
$T_{sk,i}$	Local skin temperature (°C)
$T_{sk,m,0}$	Baseline mean skin temperature (°C)
$T_{sk,m}$	Mean skin temperature (°C)
T_{water}	Water immersion temperature (°C)
t	Time (s)
U^*_{cl}	Effective local convective heat transfer coefficient ($W \cdot m^{-2} \cdot K^{-1}$)
$U^*_{E,cl}$	Effective local evaporative heat transfer coefficient ($W \cdot m^{-2} \cdot Pa^{-1}$)
V	Volume of body tissue (m^3)
v_{air}	Air velocity ($m \cdot s^{-1}$)
V_m	Muscle volume (m^3)
$\dot{V}_{O_2,r}$	Relative rate of oxygen consumption (dimensionless)
$\dot{V}_{O_2}$	Rate of oxygen consumption per body unit mass ($mL \cdot min^{-1} \cdot kg^{-1}$)
$\dot{V}_{O_2,crit}$	Critical relative rate of oxygen consumption affecting vasodilation threshold temperature (dimensionless)
$\dot{V}_{O_2,max}$	Maximal rate of oxygen consumption per body unit mass ($mL \cdot min^{-1} \cdot kg^{-1}$)
ΔT_c	Difference between current and baseline core body temperatures (°C)
$\Delta T_{c,th,Act}$	Change in vasodilation threshold temperature due to physical activity (°C)
$\Delta T_{sk,m}$	Difference between current and baseline mean skin temperatures (°C)
β	Partial heat exchange coefficient during capillary perfusion (dimensionless)
χ	Passing blood flow heat exchange efficiency (dimensionless)
ρ	Density ($kg \cdot m^{-3}$)
ρ_b	Blood density ($kg \cdot m^{-3}$)
$\dot{\omega}_b$	Blood perfusion rate ($m^3 \cdot s^{-1} \cdot m^{-3}$)

APPENDIX

Tissue Thermophysical Properties

Table A1 lists the thermophysical properties of different tissue types used in the 3-D virtual human model.

Blood-Tissue Heat Transfer Framework: Auxiliary Equations

To obtain the arterial and venous blood temperatures within a body segment i (with i = 1, 2, . . ., 12) in *Eqs. 2* and *3*, additional auxiliary equations are needed to satisfy mass conservation and temperature continuity between consecutive body segments. *Equations A1–A4* satisfy the mass flow rate continuity for arterial and venous blood flows in a body segment, as follows:

$$\dot{m}_{a,in,i} = \int \rho_b \dot{\omega}_{b,i} dV_i + \sum_{i+1}^{n} \left(\int \rho_b \dot{\omega}_{b,i} dV_i \right) \quad (A1)$$

Table A1. *Thermophysical properties of different tissue types used in the 3-D virtual human model*[a]

Tissue	ρ, kg·m^{-3}	k, W·m^{-1}·K^{-1}	c_p, J·kg^{-1}·K^{-1}	$\dot{\omega}_{b0}$, l·s^{-1}·m^{-3}	$\dot{Q}_{m0}$, W·m^{-3}
Adrenal gland	1,028	0.44	3,513	25.00	23,197
Bladder	1,086	0.52	3,581	1.41	1,312
Brainstem	1,046	0.51	3,630	9.73	11,884
Cerebrum	1,046	0.51	3,630	9.73	11,884
Cerebellum	1,045	0.51	3,653	13.40	16,373
Cerebrospinal fluid	1,007	0.57	4,095	0.00	0
Esophagus lumen	1	0.03	3,500	3.29	3,060
Esophagus wall	1,040	0.53	3,500	3.29	3,060
Eyes	1,005	0.59	4,047	0.00	0
Gallbladder	1,071	0.52	3,716	0.53	497
Gallbladder lumen	928	0.58	4,037	0.00	0
Heart	1,081	0.56	3,686	18.50	42,640
Heart lumen	1,050	0.52	3,617	0.00	0
Hypothalamus	1,045	0.55	3,696	13.30	16,231
Kidney	1,066	0.53	3,763	67.40	19,248
Large intestine lumen	1,045	0.56	3,801	0.00	0
Large intestine wall	1,088	0.54	3,654	13.90	12,894
Liver	1,055	0.51	3,600	15.50	10,713
Lungs	1,050	0.14	3,600	2.63	816
Muscle	1,085	0.42	3,768	0.34	502
Pancreas	1,087	0.51	3,164	13.90	12,914
Prostate	1,045	0.51	3,760	6.86	6,378
Skeleton-cartilage	1,100	0.49	3,568	0.64	298
Skeleton-flat	1,397	0.31	1,986	0.56	256
Skeleton-long	1,537	0.27	1,614	0.46	210
Skeleton-mandible	1,397	0.31	1,986	0.56	256
Skeleton-short	1,178	0.31	2,274	0.59	271
Skeleton-skull	1,397	0.31	1,986	0.56	256
Skeleton-vertebrae	1,178	0.31	2,274	0.59	271
Skin-dermis	1,109	0.52	3,390	1.44	1,827
Skin-epidermis	1,109	0.26	3,600	0.00	0
Small intestine lumen	1,045	0.56	3,801	0.00	0
Small intestine wall	1,030	0.49	3,595	17.60	8,185
Spinal cord	1,075	0.51	3,630	2.87	2,669
Spleen	1,089	0.53	3,630	28.30	15,755
Stomach	1,088	0.53	3,690	8.35	7,756
Stomach lumen	1,045	0.56	3,801	0.00	0
Subarachnoid space	1,007	0.57	4,096	0.00	0
Subcutaneous fat	850	0.16	2,300	0.33	282
Testis	1,082	0.52	3,778	3.60	3,348
Thymus	1,023	0.34	3,043	4.21	3,915
Trachea	1,080	0.49	3,568	0.63	585
Trachea lumen	1	0.03	1,004	0.00	0
Vertebral disc	1,100	0.49	3,568	0.64	596

[a]Obtained from Refs. 38–41.

$$\dot{m}_{a,out,i} = \dot{m}_{a,in,i} - \int \rho_b \dot{\omega}_{b,i} dV_i \quad (A2)$$

$$\dot{m}_{v,out,i} = \dot{m}_{a,out,i} \quad (A3)$$

$$\dot{m}_{v,out,i} = \dot{m}_{v,in,i} + \int \rho_b \dot{\omega}_{b,i} dV_i \quad (A4)$$

where n in *Eq. A1* denotes the number of body elements along the blood flow path, for example, $n = 4$ for the blood flowing from the heart to the shoulders, upper arms, lower arms, and hands. In *Eq. A2*, the mass flow rate of the incoming arterial blood $\dot{m}_{a,in,i}$ in the ith element is the sum total of the amount of blood perfusing the element and the downstream segments from i + 1 to n. After blood perfusion in the ith element, the resulting arterial blood $\dot{m}_{a,out,i}$ flows out to the i + 1th element. The mass flow rates for the venous return are described similarly, but in the opposite direction (Eqs. *A3 and A4*).

Likewise, *Eqs. A5–A8* satisfy the temperature continuity between body segments:

$$T_{a,in,i} = T_{a,out,i-1} \quad (A5)$$

$$T_{v,in,i} = T_{v,out,i+1} \quad (A6)$$

$$T_{a,out,i} = 2T_{a,i} - T_{a,in,i} \quad (A7)$$

$$T_{v,out,i} = 2T_{v,i} - T_{v,in,i} \quad (A8)$$

In *Eqs. A5* and *A6*, the incoming arterial and venous blood temperatures to the ith segment are based on the outgoing blood temperatures from the previous (i–1) and the next (i + 1) segments, respectively. In *Eqs. A7* and *A8*, we obtained the outgoing arterial and venous blood temperatures by assuming that the average blood temperature in a segment is an arithmetic mean of the incoming and outgoing blood temperatures (45).

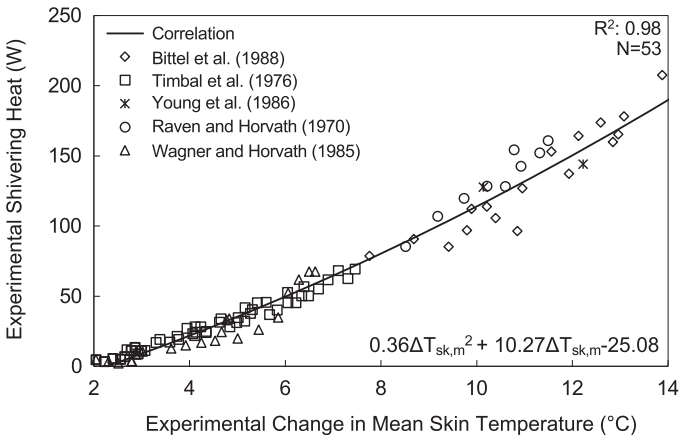

Figure A1. Correlation between experimentally observed heat due to shivering ("shivering heat") and changes in mean skin temperature obtained by collating experimental data from multiple cold-stress studies conducted in air (29, 49–51). This correlation was used as part of the input to the three-dimensional virtual human model to predict heat due to shivering for t > 30 min, when simulating cold-air exposures (see *Eq. 11*). Open symbols denote mean experimental values (n = 53), whereas the solid line denotes the computed correlation function. R^2, coefficient of determination; $\Delta T_{sk,m}$, change in mean skin temperature from an initial thermoneutral state. *N*, number of subjects.

Shivering Heat for Air Exposures

Figure A1 shows the correlation between experimentally observed heat due to shivering and changes in mean skin temperature data from multiple cold-stress studies conducted in air (29, 54–56).

Model Validation for Heat Stress

Figures A2 and A3 show model validation of the core body temperature under heat-stress and exertional conditions.

Skin Blood Flow Model Equations

In the extended virtual human model, we implemented the SBF mechanism proposed by Wissler (15, 48), which assumes a multiplicative combination of the thermoregulatory vasoconstriction and vasodilation mechanisms, as follows:

$$SBF_i = SBF_{i,0} \times CVCM \times CVCL \times AVD \times C_{sbf} \quad (A9)$$

where SBF_i and $SBF_{i,0}$ denote the local and corresponding basal skin blood perfusion rate in the ith body segment, respectively, CVCM and CVCL represent the centrally and locally mediated cutaneous vasoconstriction, respectively, AVD denotes the active vasodilation, and C_{sbf} represents the circadian rhythmicity of the SBF.

We defined CVCM to be a function of the mean skin temperature $T_{sk,m}$, as follows:

$$CVCM = \frac{1.422 + \tanh\left[0.275(T_{sk,m} - 32)\right]}{2.018} \quad (A10)$$

where tanh denotes the hyperbolic tangent function. Similarly, we defined CVCL to be a function of the local skin temperature $T_{sk,i}$. We tabulated the data from Wissler (15), shown in Fig. A4, to represent CVCL($T_{sk,i}$) in our model.

AVD was based on the core body temperature T_c, the mean skin temperature, and the physical activity intensity estimated by the rate of oxygen consumption $\dot{V}_{O_2}$. In the model, active vasodilation occurs when T_c increases above a specific threshold temperature $T_{c,th}$, as follows:

$$T_{c,th} = T_{c,th,0} - 0.05(T_{sk,m} - 33) + \Delta T_{c,th,Act} \quad (A11)$$

where $T_{c,th,0}$ represents the threshold core body temperature for a resting individual when the mean skin temperature equals 33°C. According to Wissler, there are two contributions to AVD due to *1*) environmental heat stress and *2*) physical activity. Vasodilation, considering the effects of only environmental heat stress, was defined as follows:

$$AVD^* = \begin{cases} 1, & T_c \le T_{c,th} \\ 1 + 8.25(T_c - T_{c,th}), & T_c > T_{c,th} \end{cases} \quad (A12)$$

Physical activity affects AVD by increasing the vasodilation threshold temperature $T_{c,th}$ in *Eq. A11*, depending on the intensity of the physical activity:

$$\Delta T_{c,th,Act} = 1.41\Delta V^2 - 0.19\Delta V + 0.01\Delta V \quad (A13)$$

$$\text{with} \quad \Delta V = \frac{\dot{V}_{O_2,r} - \dot{V}_{O_2,crit}}{1.0 - \dot{V}_{O_2,crit}}$$

where $\dot{V}_{O_2,r}$ denotes the ratio of the rate of oxygen consumption $\dot{V}_{O_2}$ during physical activity over the maximal oxygen consumption rate $\dot{V}_{O_2,max}$ and $\dot{V}_{O_2,crit}$ represents the critical $\dot{V}_{O_2,r}$ for which physical activity starts to affect $T_{c,th}$, and is defined as:

$$\dot{V}_{O_2,crit} = \begin{cases} 0.5, & T_{sk,m} \le 33°C \\ \max(0,\ (0.5 - 0.1(T_{sk,m} - 33°C))), & T_{sk,m} \ge 33°C \end{cases} \quad (A14)$$

After including the effect of physical activity, the net expression describing AVD in *Eq. A9* depends on the model's computation of $\dot{V}_{O_2,r}$ and Tc and is given by:

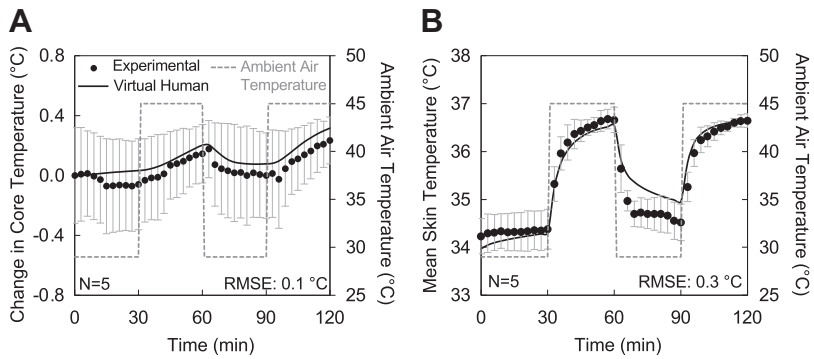

Figure A2. Model validation of the core body temperature (*A*) and the mean skin temperature (*B*) for an environmental heat-stress study in which five subjects wearing shorts sat in an environmental chamber for 120 min, whereas the air temperature changed drastically from neutral to very hot (29°C–45°C to 29°C–45°C and 40% relative humidity) (*study 8*, Table 1). The filled circles represent the average of the measured changes in core body temperature (*A*) or the mean skin temperature (*B*), the vertical gray bars indicate two standard errors of the mean, the gray dashed lines represent the ambient air temperature, and the solid black lines denote the three-dimensional virtual human model predictions for core body temperature change (*A*) or the mean skin temperature (*B*). RMSE, root mean squared error. *N*, number of subjects.

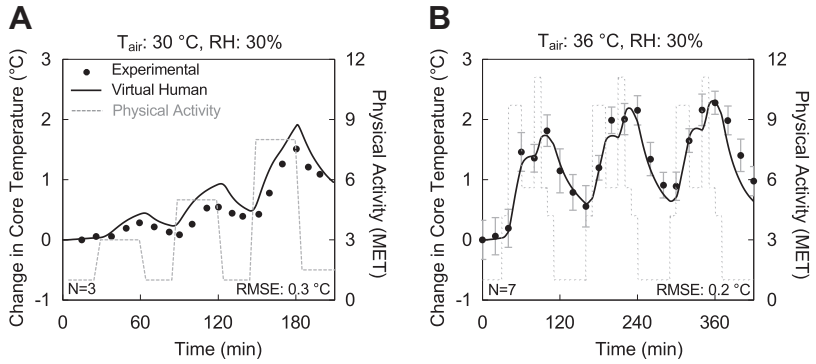

Figure A3. Model validation of the core body temperature for two exertional and environmental heat-stress conditions in which three subjects wearing shorts pedaled on a bicycle ergometer at three different intensities for 210 min at 30°C and 30% relative humidity (RH; *A*) (*study 9*, Table 1) and seven subjects wearing a T-shirt and shorts ran on a treadmill while performing three strenuous exercise bouts of varying intensities for 420 min at 36°C and 30% RH (*B*; *study 10*, Table 1). The filled circles represent the average of the measured changes in core body temperature, the vertical gray bars indicate two standard errors of the mean, the gray dashed lines represent the physical activity level, and the solid black lines denote the three-dimensional virtual human model predictions for core temperature change. MET, metabolic equivalent; RMSE, root mean squared error; T_{air}, ambient air temperature. *N*, number of subjects.

$$AVD = \begin{cases} AVD^*, \text{ for } \dot{V}_{O_2,r} > 0.4 \text{ and } T_c \le 38^\circ C, \ \dot{V}_{O_2,r} < 0.4 \text{ and } T_c \le 38^\circ C, \ \dot{V}_{O_2,r} < 0.4 \text{ and } T_c \ge 38^\circ C \\ AVD^* \times [1 - 0.25(T_c - 38^\circ C)], \text{ for } 0.4 < \dot{V}_{O_2,r} < 0.9 \text{ and } T_c > 38^\circ C \\ 0.5AVD^*, \text{ for } \dot{V}_{O_2,r} > 0.9 \text{ and } T_c > 38^\circ C \end{cases} \quad (A15)$$

Clothing Model

We represented the heat transfer between the external environment and the skin surface through the clothing layer, using the following equation:

$$-k\frac{\partial T_{sk}}{\partial n} = U^*_{cl}(T_{sk} - T_{amb}) \quad (A16)$$

where T_{amb} denotes the ambient operative temperature, and U^*_{cl} denotes the local effective heat-transfer coefficient, including the effects of convective and radiative heat transfer between the skin and the external environment, as well as the effect of clothing:

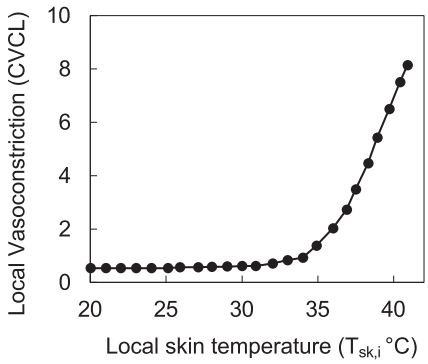

Figure A4. Local vasoconstriction as a function of local skin temperature (22).

$$U^*_{cl} = \frac{1}{\sum_{m=1}^{M}(I^*_{cl})_m + \frac{1}{f^*_{cl}(h_c + h_r)}} \quad (A17)$$

where I^*_{cl} denotes the local thermal resistance of the mth clothing layer, f^*_{cl} indicates the local clothing area factor of the outermost clothing, h_c denotes the convective heat transfer coefficient, h_r represents the radiant heat transfer coefficient, and M denotes the total number of clothing layers. The total heat transfer due to evaporation and diffusion of sweat from the skin is given by (40)

$$\frac{\lambda_{H_2O}}{A_{sk}}\frac{dm_{sw}}{dt} = U^*_{E,cl}(p_{sk} - p_{air}) + \frac{p_{osk,\ sk} - p_{sat}}{R_{E,sk}} \quad (A18)$$

where $U^*_{E,cl}$ denotes the evaporative coefficient, p_{sk} indicates the partial water vapor pressure at the skin surface, p_{air} represents the partial water vapor pressure of the surrounding air, λ_{H_2O} = 2,260 kJ·kg^{-1} refers to the heat of vaporization of water, A_{sk} indicates the skin surface area, $p_{osk,sat}$ denotes the saturated partial water vapor pressure within the outer skin layer, and $1/R_{E,sk}$ = 0.003 W·m^{-2}·Pa^{-1} represents the moisture permeability of the skin. The evaporative coefficient $U^*_{E,cl}$ accounts for the effect of clothing as

$$U^*_{E,cl} = \frac{L_a}{\sum_{m=1}^{M}\left(\frac{I^*_{cl}}{i^*_{cl}}\right)_m + \frac{1}{f^*_{cl}\cdot h_c}} \quad (A19)$$

where I^*_{cl} represents the local thermal resistance of the mth clothing, i^*_{cl} represents the local, garment-oriented, moisture permeability index, L_a refers to the Lewis constant for air, f^*_{cl} denotes the local clothing area factor, and h_c represents the

convective heat-transfer coefficient. *Equations A17* and *A19* implicitly account for air gaps between clothing layers when measured values of I_{cl}^{*} and $i_{cl}^{*}$of a clothing ensemble are available.

DATA AVAILABILITY

Experimental data and predictions presented in this manuscript will be made available through a written request (including a summary of the planned research) to the corresponding author.

ACKNOWLEDGMENTS

We acknowledge support from the DoD High Performance Computing Modernization Program for use of their supercomputing centers.

GRANTS

This work was supported by the US Army Medical Research and Development Command. The Henry M. Jackson Foundation was supported under Contract No. W81XWH20C0031.

DISCLAIMERS

The opinions and assertions contained herein are the private views of the authors and are not to be construed as official or as reflecting the views of the US Army, the US Department of Defense (DoD), or The Henry M. Jackson Foundation for the Advancement of Military Medicine, Inc. (HJF). This paper has been approved for public release with unlimited distribution.

DISCLOSURES

No conflicts of interest, financial or otherwise, are declared by the authors.

AUTHOR CONTRIBUTIONS

T.G., R.H., G.U., and J.R. conceived and designed research; T.G., R.H., and G.U. developed the model; T.G. and R.H. performed the simulations; T.G., R.H., G.U., and J.R. interpreted the results of the simulations; T.G. drafted the manuscript; J.E.R. and J.R. edited the manuscript; T.G., R.H., G.U., J.E.R., and J.R. approved the final version of the manuscript.

REFERENCES

1. **Xiang J**, **Bi P**, **Pisaniello D**, **Hansen A.** Health impacts of workplace heat exposure: an epidemiological review. *Ind Health* 52: 91–101, 2014.
2. **Shenaq DS**, **Gottlieb LJ.** Cold injuries. *Hand Clin* 33: 257–267, 2017. doi:10.1016/j.hcl.2016.12.003.
3. **Armed Forces Health Surveillance Division.** Update: heat illness, active component, U.S. Armed Forces, 2019. *MSMR* 27: 4–9, 2020.
4. **Armed Forces Health Surveillance Division.** Update: cold weather injuries, active and reserve components, U.S. Armed Forces, July 2015–June 2020. *MSMR* 27: 15–24, 2020.
5. **Varghese GM**, **John G**, **Thomas K**, **Abraham OC**, **Mathai D.** Predictors of multi-organ dysfunction in heatstroke. *Emerg Med J* 22: 185–187, 2005. doi:10.1136/emj.2003.009365.
6. **Lantry J**, **Dezman Z**, **Hirshon JM.** Pathophysiology, management and complications of hypothermia. *Br J Hosp Med (Lond)* 73: 31–37, 2012. doi:10.12968/hmed.2012.73.1.31.
7. **Danielsson U.** Windchill and the risk of tissue freezing. *J Appl Physiol (1985)* 81: 2666–2673, 1996. doi:10.1152/jappl.1996.81.6.2666.
8. **Keane M.** Triad of death: the importance of temperature monitoring in trauma patients. *Emerg Nurse* 24: 19–23, 2016.
9. **Knapik JJ**, **Reynolds KL**, **Castellani JW.** Frostbite: pathophysiology, epidemiology, diagnosis, treatment, and prevention. *J Spec Oper Med* 20: 123–135, 2020. doi:10.55460/pdx9-bg8g.
10. **Haslam RA**, **Parsons KC.** Using computer-based models for predicting human thermal responses to hot and cold environments. *Ergonomics* 37: 399–416, 1994. doi:10.1080/00140139408963659.
11. **Fu M**, **Weng W**, **Chen W**, **Luo N.** Review on modeling heat transfer and thermoregulatory responses in human body. *J Therm Biol* 62: 189–200, 2016. doi:10.1016/j.jtherbio.2016.06.018.
12. **Katić K**, **Li R**, **Zeiler W.** Thermophysiological models and their applications: a review. *Build Environ* 106: 286–300, 2016. doi:10.1016/j.buildenv.2016.06.031.
13. **Xu X**, **Tikuisis P.** Thermoregulatory modeling for cold stress. *Compr Physiol* 4: 1057–1081, 2014. doi:10.1002/cphy.c130047.
14. **Wissler EH.** Temperature distribution in the body. In: *Human Temperature Control*. Berlin, Heidelberg: Springer, 2018, p. 265–287.
15. **Wissler EH.** Whole-body human thermal models. In: *Advances in Numerical Heat Transfer*, Volume 3. Boca Raton, FL: CRC Press, 2009, p. 257–306.
16. **Chen F**, **Liu ZY**, **Holmér I.** Hand and finger skin temperatures in convective and contact cold exposure. *Eur J Appl Physiol Occup Physiol* 72: 372–379, 1996. doi:10.1007/BF00599699.
17. **Christ A**, **Kainz W**, **Hahn EG**, **Honegger K**, **Zefferer M**, **Neufeld E**, **Rascher W**, **Janka R**, **Bautz W**, **Chen J**, **Kiefer B**, **Schmitt P**, **Hollenbach H-P**, **Shen J**, **Oberle M**, **Szczerba D**, **Kam A**, **Guag JW**, **Kuster N.** The Virtual Family–development of surface-based anatomical models of two adults and two children for dosimetric simulations. *Phys Med Biol* 55: N23–N38, 2010. doi:10.1088/0031-9155/55/2/N01.
18. **Moore SM**, **McIntosh RL**, **Iskra S**, **Wood AW.** Modeling the effect of adverse environmental conditions and clothing on temperature rise in a human body exposed to radio frequency electromagnetic fields. *IEEE Trans Biomed Eng* 62: 627–637, 2015. doi:10.1109/TBME.2014.2362517.
19. **Werner J**, **Buse M.** Temperature profiles with respect to inhomogeneity and geometry of the human body. *J Appl Physiol (1985)* 65: 1110–1118, 1988. doi:10.1152/jappl.1988.65.3.1110.
20. **Unnikrishnan G**, **Hatwar R**, **Hornby S**, **Laxminarayan S**, **Gulati T**, **Belval LN**, **Giersch GEW**, **Kazman JB**, **Casa DJ**, **Reifman J.** A 3-D virtual human thermoregulatory model to predict whole-body and organ-specific heat-stress responses. *Eur J Appl Physiol* 121: 2543–2562, 2021. doi:10.1007/s00421-021-04698-1.
21. **Castellani MP**, **Rioux TP**, **Castellani JW**, **Potter AW**, **Xu X.** A geometrically accurate 3 dimensional model of human thermoregulation for transient cold and hot environments. *Comput Biol Med* 138: 104892, 2021. doi:10.1016/j.compbiomed.2021.104892.
22. **Nelson DA**, **Charbonnel S**, **Curran AR**, **Marttila EA**, **Fiala D**, **Mason PA**, **Ziriax JM.** A high-resolution voxel model for predicting local tissue temperatures in humans subjected to warm and hot environments. *J Biomech Eng* 131: 041003, 2009. doi:10.1115/1.3002765.
23. **Zhang M**, **Li R**, **Li J**, **Wang F**, **Subramaniam S**, **Lang J**, **Passalacqua A**, **Song G.** A 3D multi-segment thermoregulation model of the hand with realistic anatomy: development, validation, and parametric analysis. *Build Environ* 201: 107964, 2021. doi:10.1016/j.buildenv.2021.107964.
24. **Brinck H**, **Werner J.** Efficiency function: improvement of classical bioheat approach. *J Appl Physiol (1985)* 77: 1617–1622, 1994. doi:10.1152/jappl.1994.77.4.1617.
25. **Ducharme MB**, **Tikuisis P.** In vivo thermal conductivity of the human forearm tissues. *J Appl Physiol (1985)* 70: 2682–2690, 1991. doi:10.1152/jappl.1991.70.6.2682.
26. **Paul AK**, **Zachariah S**, **Zhu L**, **Banerjee RK.** Predicting temperature changes during cold water immersion and exercise scenarios: application of a tissue–blood interactive whole-body model. *Numeri Heat Transf A Appl* 68: 598–618, 2015. doi:10.1080/10407782.2014.994417.
27. **Tikuisis P.** Prediction of the thermoregulatory response for clothed immersion in cold water. *Eur J Appl Physiol Occup Physiol* 59: 334–341, 1989. doi:10.1007/BF02389807.
28. **Tikuisis P**, **Gonzalez RR**, **Pandolf KB.** Thermoregulatory model for immersion of humans in cold water. *J Appl Physiol (1985)* 64: 719–727, 1988. doi:10.1152/jappl.1988.64.2.719.

29. **Bittel JH**, **Nonotte-Varly C**, **Livecchi-Gonnot GH**, **Savourey GL**, **Hanniquet AM.** Physical fitness and thermoregulatory reactions in a cold environment in men. *J Appl Physiol (1985)* 65: 1984–1989, 1988. doi:10.1152/jappl.1988.65.5.1984.
30. **Inoue Y**, **Nakao M**, **Araki T**, **Ueda H.** Thermoregulatory responses of young and older men to cold exposure. *Europ J Appl Physiol Occup Physiol* 65: 492–498, 1992. doi:10.1007/BF00602354.
31. **Timbal J**, **Boutelier C**, **Loncle M**, **Bougues L.** Comparison of shivering in man exposed to cold in water and in air. *Pflugers Arch* 365: 243–248, 1976. doi:10.1007/BF01067024.
32. **Castellani JW**, **Young AJ**, **Sawka MN**, **Pandolf KB.** Human thermoregulatory responses during serial cold-water immersions. *J Appl Physiol (1985)* 85: 204–209, 1998. doi:10.1152/jappl.1998.85.1.204.
33. **Hayward JS**, **Eckerson JD**, **Collis ML.** Thermoregulatory heat production in man: prediction equation based on skin and core temperatures. *J Appl Physiol Respir Environ Exerc Physiol* 42: 377–384, 1977. doi:10.1152/jappl.1977.42.3.377.
34. **Lee DT**, **Toner MM**, **McArdle WD**, **Vrabas IS**, **Pandolf KB.** Thermal and metabolic responses to cold-water immersion at knee, hip, and shoulder levels. *J Appl Physiol (1985)* 82: 1523–1530, 1997. doi:10.1152/jappl.1997.82.5.1523.
35. **Stolwijk JAJ.** *A Mathematical Model of Physiological Temperature Regulation in Man*. Washington D.C.: National Aeronautics and Space Administration, 1971.
36. **Yang J**, **Weng W**, **Zhang B.** Experimental and numerical study of physiological responses in hot environments. *J Therm Biol* 45: 54–61, 2014. doi:10.1016/j.jtherbio.2014.07.010.
37. **Nelson DA**, **Curlee JS**, **Curran AR**, **Ziriax JM**, **Mason PA.** Determining localized garment insulation values from manikin studies: computational method and results. *Eur J Appl Physiol* 95: 464–473, 2005. doi:10.1007/s00421-005-0033-4.
38. **Tikuisis P**, **Ducharme MB.** Finite-element solution of thermal conductivity of muscle during cold water immersion. *J Appl Physiol (1985)* 70: 2673–2681, 1991. doi:10.1152/jappl.1991.70.6.2673.
39. **Buse M**, **Werner J.** Closed loop control of human body temperature: results from a one-dimensional model. *Biol Cybern* 61: 467–475, 1989. doi:10.1007/BF02414908.
40. **Fiala D**, **Lomas KJ**, **Stohrer M.** A computer model of human thermoregulation for a wide range of environmental conditions: the passive system. *J Appl Physiol (1985)* 87: 1957–1972, 1999. doi:10.1152/jappl.1999.87.5.1957.
41. **Mcintosh RL**, **Anderson V.** A comprehensive tissue properties database provided for the thermal assessment of a human at rest. *Biophys Rev Lett* 05: 129–151, 2010. doi:10.1142/S1793048010001184.
42. **Hasgall PA**, **Di Gennaro F**, **Baumgartner C**, **Neufeld E**, **Lloyd B**, **Gosselin MC**, **Payne D**, **Klingenböck A**, **Kuster N.** *IT'IS database for thermal and electromagnetic parameters of biological tissues*, Version 4.0. 2018. doi:10.13099/VIP21000-04-0.
43. **Weinbaum S**, **Xu LX**, **Zhu L**, **Ekpene A.** A new fundamental bioheat equation for muscle tissue: part I-blood perfusion term. *J Biomech Eng* 119: 278–288, 1997. doi:10.1115/1.2796092.
44. **Salloum M**, **Ghaddar N**, **Ghali K.** A new transient bioheat model of the human body and its integration to clothing models. *Int J Therm Sci* 46: 371–384, 2007. doi:10.1016/j.ijthermalsci.2006.06.017.
45. **Shitzer A**, **Stroschein LA**, **Vital P**, **Gonzalez RR**, **Pandolf KB.** Numerical analysis of an extremity in a cold environment including countercurrent arterio-venous heat exchange. *J Biomech Eng* 119: 179–186, 1997. doi:10.1115/1.2796078.
46. **Fiala D**, **Lomas KJ**, **Stohrer M.** Computer prediction of human thermoregulatory and temperature responses to a wide range of environmental conditions. *Int J Biometeorol* 45: 143–159, 2001. doi:10.1007/s004840100099.
47. **Fiala D**, **Havenith G**, **Bröde P**, **Kampmann B**, **Jendritzky G.** UTCI-Fiala multi-node model of human heat transfer and temperature regulation. *Int J Biometeorol* 56: 429–441, 2012. doi:10.1007/s00484-011-0424-7.
48. **Wissler EH.** A quantitative assessment of skin blood flow in humans. *Eur J Appl Physiol* 104: 145–157, 2008. doi:10.1007/s00421-008-0697-7.
49. **El Kadri M**, **De Oliveira F**, **Inard C**, **Demouge F.** New neurophysiological human thermal model based on thermoreceptor responses. *Int J Biometeorol* 64: 2007–2017, 2020. doi:10.1007/s00484-020-01990-1.
50. **Wissler EH.** Whole-body human thermal modeling, an alternative to immersion in cold water and other unpleasant endeavors. *J Heat Transfer* 134: 031019, 2012. doi:10.1115/1.4005155.
51. **Xu X**, **Rioux TP**, **MacLeod T**, **Patel T**, **Rome MN**, **Potter AW.** Measured body composition and geometrical data of four "virtual family" members for thermoregulatory modeling. *Int J Biometeorol* 61: 477–486, 2017. doi:10.1007/s00484-016-1227-7.
52. **Wissler EH.** Heat and mass transfer from the skin and clothing. In: *Human Temperature Control*. Berlin, Heidelberg: Springer, 2018, p. 337–383.
53. **de Dear RJ**, **Arens E**, **Hui Z**, **Oguro M.** Convective and radiative heat transfer coefficients for individual human body segments. *Int J Biometeorol* 40: 141–156, 1997. doi:10.1007/s004840050035.
54. **Raven PR**, **Horvath SM.** Variability of physiological parameters of unacclimatized males during a two-hour cold stress of 5°C. *Int J Biometeorol* 14: 309–320, 1970. doi:10.1007/BF01742075.
55. **Wagner JA**, **Horvath SM.** Influences of age and gender on human thermoregulatory responses to cold exposures. *J Appl Physiol (1985)* 58: 180–186, 1985. doi:10.1152/jappl.1985.58.1.180.
56. **Young AJ**, **Muza SR**, **Sawka MN**, **Gonzalez RR**, **Pandolf KB.** Human thermoregulatory responses to cold air are altered by repeated cold water immersion. *J Appl Physiol (1985)* 60: 1542–1548, 1986. doi:10.1152/jappl.1986.60.5.1542.
57. **Tikuisis P**, **Giesbrecht GG.** Prediction of shivering heat production from core and mean skin temperatures. *Eur J Appl Physiol Occup Physiol* 79: 221–229, 1999. doi:10.1007/s004210050499.
58. **Bell DG**, **Tikuisis P**, **Jacobs I.** Relative intensity of muscular contraction during shivering. *J Appl Physiol (1985)* 72: 2336–2342, 1992. doi:10.1152/jappl.1992.72.6.2336.
59. **Tikuisis P**, **Bell DG**, **Jacobs I.** Shivering onset, metabolic response, and convective heat transfer during cold air exposure. *J Appl Physiol (1985)* 70: 1996–2002, 1991. doi:10.1152/jappl.1991.70.5.1996.
60. **Kingma BR**, **Frijns AJH**, **Schellen L**, **van Marken Lichtenbelt WD.** Beyond the classic thermoneutral zone: including thermal comfort. *Temperature (Austin)* 1: 142–149, 2014.
61. **Ferreira MS**, **Yanagihara JI.** A transient three-dimensional heat transfer model of the human body. *Int J Heat Mass Transf* 36: 718–724, 2009. doi:10.1016/j.icheatmasstransfer.2009.03.010.
62. **Giesbrecht GG**, **Goheen MS**, **Johnston CE**, **Kenny GP**, **Bristow GK**, **Hayward JS.** Inhibition of shivering increases core temperature afterdrop and attenuates rewarming in hypothermic humans. *J Appl Physiol (1985)* 83: 1630–1634, 1997. doi:10.1152/jappl.1997.83.5.1630.
63. **Vanggaard L**, **Eyolfson D**, **Xu X**, **Weseen G**, **Giesbrecht GG.** Immersion of distal arms and legs in warm water (AVA rewarming) effectively rewarms mildly hypothermic humans. *Aviat Space Environ Med* 70: 1081–1088, 1999.
64. **Keller KH**, **Seiler JL Jr.** An analysis of peripheral heat transfer in man. *J Appl Physiol* 30: 779–786, 1971. doi:10.1152/jappl.1971.30.5.779.
65. **Weinbaum S**, **Jiji LM**, **Lemons DE.** Theory and experiment for the effect of vascular microstructure on surface tissue heat transfer-part I: anatomical foundation and model conceptualization. *J Biomech Eng* 106: 321–330, 1984. doi:10.1115/1.3138501.
66. **Potkanowicz ES**, **Caine-Bish N**, **Otterstetter R**, **Glickman EL.** Age effects on thermal, metabolic, and perceptual responses to acute cold exposure. *Aviat Space Environ Med* 74: 1157–1162, 2003.
67. **JBODY, Energy Simulation Solutions Ltd.** Loughborough, UK. https://app.ensims.com/jbody/ [2022 Feb 2].
68. **Castellani JW**, **Yurkevicius BR**, **Jones ML**, **Driscoll TJ**, **Cowell CM**, **Smith L**, **Xu X**, **O'Brien C.** Effect of localized microclimate heating on peripheral skin temperatures and manual dexterity during cold exposure. *J Appl Physiol (1985)* 125: 1498–1510, 2018. doi:10.1152/japplphysiol.00513.2018.
69. **Holmér I.** Assessment of cold stress by calculation of required clothing insulation—IREQ. In: *Elsevier Ergonomics Book Series, Volume 3: Environmental Ergonomics—The Ergonomics of Human Comfort Health and Performance in the Thermal Environment.* Amsterdam, The Netherlands: Elsevier, 2005, p. 503–506.
70. **Xu X**, **Rioux TP**, **Gonzalez J**, **Hansen EO**, **Castellani JW**, **Santee WR**, **Karis AJ**, **Potter AW.** A digital tool for prevention and management of cold weather injuries—Cold Weather Ensemble Decision Aid (CoWEDA). *Int J Biometeorol* 65: 1415–1426, 2021. doi:10.1007/s00484-021-02113-0.
71. **Dutta R**, **Kulkarni K**, **Steinman AM**, **Gardiner PF**, **McDonald GK**, **Giesbrecht GG.** Human responses to 5 heated hypothermia wrap

systems in a cold environment. *Wilderness Environ Med* 30: 163–176, 2019. doi:10.1016/j.wem.2019.02.006.

72. **Ginsberg MD**, **Globus MY**, **Dietrich WD**, **Busto R.** Temperature modulation of ischemic brain injury—a synthesis of recent advances. *Progr Brain Res* 96: 13–22, 1993. doi:10.1016/s0079-6123(08)63256-2.
73. **Tipton MJ**, **Collier N**, **Massey H**, **Corbett J**, **Harper M.** Cold water immersion: kill or cure? *Exp Physiol* 102: 1335–1355, 2017. doi:10.1113/EP086283.
74. **Kimberger O**, **Kurz A.** Thermoregulatory management for mild therapeutic hypothermia. *Best Pract Res Clin Anaesthesiol* 22: 729–744, 2008. doi:10.1016/j.bpa.2007.11.002.
75. **Urbano LA**, **Oddo M.** Therapeutic hypothermia for traumatic brain injury. *Curr Neurol Neurosci Rep* 12: 580–591, 2012. doi:10.1007/s11910-012-0304-5.
76. **Dennis BH**, **Eberhart RC**, **Dulikravich GS**, **Radons SW.** Finite-element simulation of cooling of realistic 3-D human head and neck. *J Biomech Eng* 125: 832–840, 2003. doi:10.1115/1.1634991.
77. **Kalra M**, **Bahrami M**, **Sparrey CJ.** The effects of physiological thermoregulation on the efficacy of surface cooling for therapeutic hypothermia. *Med Biol Eng Comput* 53: 205–213, 2015. doi:10.1007/s11517-014-1229-8.
78. **Gibbons TD**, **Tymko MM**, **Thomas KN**, **Wilson LC**, **Stembridge M**, **Caldwell HG**, **Howe CA**, **Hoiland RL**, **Akerman AP**, **Dawkins TG**, **Patrician A**, **Coombs GB**, **Gasho C**, **Stacey BS**, **Ainslie PN**, **Cotter JD.** Global REACH 2018: The influence of acute and chronic hypoxia on cerebral haemodynamics and related functional outcomes during cold and heat stress. *J Physiol* 598: 265–284, 2020. doi:10.1113/jp278917.